ARENA 2015 RND086

From single to multiple wave energy converters: Cost reduction through location and configuration optimisation

THE UNIVERSITY OF WESTERN AUSTRALIA

Final Report – October 2021

The University of Western Australia

The Wave Energy Research Centre

https://marineresearch-gs.com/wave-energy-research-centre/

Acknowledgements

The project was undertaken under the conbined financial support of the Australian Renewable Energy Agency (ARENA) Research and Development programme (ARENA 2015 RND086) and the Unviversity of Western Australia.

https://arena.gov.au/projects/wave-energy-cost-reduction-through-location-and-configuration-optimisation/

Contributing authors

Professor Christophe Gaudin

Daniel Raj David

Yongmin Cai

A/Professor Jeff Hansen

Professor Fraser Bransby

Dr Dirk Rijnsdorp

Professor Ryan Lowe

A/Professor Conleth O'Loughlin

Ting Lu

Dr Marco Uzielli

Dr Michael O'Neill

Collaborating partners

Carnegie Clean Energy Ltd

University of Florence

Citation

Gaudin C., David D.R., Cai Y., Hansen J.E., Bransby M.F., Rijnsdorp D.P, Lowe R.J., O'Loughlin C.D., Lu T., Uzielli M., O'Neill M. (2021). From single to multiple wave energy converters: Cost reduction through location and configuration optimisation. Final Report. The University of Western Australia. 65 p.

Copyright

Disclaimer

Contents

List of Figures

List of Tables

1. Executive summary

The University of Western Australia, in collaboration with Carnegie Clean Energy and with the support of the Australian Renewable Energy Agency has undertaken a four-year research programme aimed at developing ocean engineering solutions to reduce the levelised cost of wave energy.

The research programme focused on developing a multidisciplinary optimisation approach that considers not only maximisation of the power production but minimisation of cabling and foundation infrastructure costs. Specifically, the approach enables the identification of the optimal location and configuration of an array of wave energy converters as a function of wave resources, seabed characteristics and potential coastal impacts. In this context, the optimal location is the location that exhibits the lowest ratio of cost of infrastructure to mean power output.

The approach developed is illustrated by exploring the virtual development of an array of twenty Carnegie Clean Energy's CETO6 wave energy converters in Torbay, near Albany, Western Australia. The CETO6 device is a point absorber wave energy converter with a power rating of 1 MW.

The innovation achieved by this research programme is twofold: in the holistic consideration of multiple parameters to identify the optimal array location, and in the techniques developed to optimise array configuration and foundation design.

While the outcomes and savings demonstrated are specific to the virtual array, site and ground conditions considered, the approach and the techniques developed can be used for any potential wave energy farm, but also for fixed or floating wind farms.

1.1. The challenge

Even in a COVID world, energy demand is still expected to rise in the coming decades. With the threat generated by climate change, this demand must be met by clean and sustainable energy and significant development must be undertaken worldwide to reach the target established collectively by the 2021 Paris Agreement.

While wind (both onshore and offshore) and solar energy have reached commercial maturity, wave energy has not, despite abundant resources and significant potential. This is due to multiple factors, the most important one being the high levelised cost of wave energy, resulting from the maturity of the technology, which still requires development and from the specificity of the technology, which is meant to be deployed in high energy, therefore challenging, environments where survivability during extreme conditions may induce additional costs.

However, wave energy has significant potential and will no doubt be part of the future energy mix. The diversity of technology makes it suitable for a broad range of market opportunities, from low demand high-cost markets to high demand low-cost markets. As the technology progresses and economies of scale are achieved, the levelised cost of wave energy is expected to follow a similar trend to that of wind energy, which has seen a reduction by a factor of ten over four decades.

Cost reduction will be achieved through economy of scale, technological development, both in the energy conversion and in the associated infrastructure, but also through innovative design approaches that consider holistically all the variables of the problem and particularities of wave energy.

1.2. Our response

This project focuses on the specific aspects of infrastructure of wave energy farms associated with cabling and foundation engineering, which may represent 20-30% of the total cost of a development. In both case, industry practices are inherited from the offshore oil and gas industry which, despite evident knowledge and technology transfer, may not be fully appropriate to wave energy developments. This is due to different economic rationales, the high conservatism evidently required for manned oil and gas infrastructure, but also to the particularities of wave energy converters, which are not adequately considered in design codes and guidelines, notably with respect to hydrodynamic loadings on mooring lines and foundations.

This presents a potential cost-saving opportunity that can be achieved by advancing the scientific knowledge of wave energy converters to generate design optimisation approaches and by developing innovative approaches that are specific to this type of device.

Specifically, in the project we have:

1. Developed a phase-resolving wave model that incorporates WECs and can be used to understand WEC array dynamics, power production, and quantify downstream impacts including modification to coastal processes.
2. Developed a design methodology for piles (the type of foundations favoured for the type of wave energy converter investigated here) that accounts for the specific loading regimes generated by point-absorber type wave energy converters and for which no guidelines currently exist.
3. Developed a site investigation optimisation technique that calculates foundation reliability as a function of the soil variability and uncertainty, hence assisting in identifying the appropriate level of site investigation for a given site that minimises installed foundation cost.
4. Developed a multi-objective optimisation technique that optimises array configuration as a function of wave resources, power take off performance and cabling arrangement.
5. Integrated the innovations listed above into a holistic approach that balances these variables to identify the optimal location and configuration of a wave energy farm that results in the minimum cost to power ratio.

The outcomes of this approach were quantified for a virtual development of twenty CETO 6 wave energy converters in Torbay, near Albany, WA, by comparing the cost to power ratio of a base case designed following industry practice with an optimised case integrating all the developments listed above.

1.3. Key findings

The key findings consist in two components: the demonstrated cost reduction generated for the example case considered in this project and the innovations achieved whilst developing this new approach.

The former was estimated using a metric that can be readily compared between the base case and the optimised case: the cost of cabling and foundation infrastructure divided by the mean power output, hereafter called the normalised cost in $/MW. This is not a typical metric and it cannot be compared with capital cost figures used in other energy generation technologies, but it is meaningful for the comparison undertaken here.

For the virtual development of a farm of twenty CETO 6 wave energy converters in Torbay, a reduction of the normalised cost defined above of about 23% was achieved through the optimisation techniques developed. This value of reduction is specific for the case considered here and the assumptions made with respect to our costing model and the seabed conditions, but the approach is universal, and can be adopted for any wave energy development. The saving achieved will depend on many different variables specific to the device and the location of the development, but they are expected to be in the same order of magnitude.

With respect to the optimisation techniques developed, the key findings are:

1. A multi-objective optimisation methodology was developed to allow developers to optimise a WEC array for power production and a range of factors that contribute to cost. The outcomes of this new method present developers with a range of WEC array arrangements with each having a differing ratio of power to cost. With this quantitative information developers can make informed decision about the trade-offs between maximising power production and project capital and operational costs.
2. With modifications to the phase-resolving wave-flow model SWASH to realistically incorporate the CETO6 device, including the absorption, scattering, and diffraction of wave energy, we were able to accurately estimate the downstream impacts of WEC arrays including potential coastal impacts. An estimate of the coastal impacts derived from a wide range of simulations was incorporated into the multi-objective optimisation.
3. An approach has been developed to rationally select design lines to achieve a target probability of failure of an anchor pile, based on the amount of information known about the seabed conditions and the proximity of the pile from the nearest CPT. This approach allows cost-benefit calculations to be made to judge the effect of increasing the number of CPTs in order to reduce the maximum distance between sampled locations and the piles and/or to quantify the horizontal scale of fluctuation of the seabed. This allows the effect of different site investigation strategies (i.e. selection of the number of investigated locations and their positioning) to be explored and the approach which gives the lowest installed cost of the foundations to be selected. This approach will result in a reduction in foundation costs.
4. For a rigid pile foundation embedded in sand, the monotonic capacity under tensile inclined loading for load inclination between 10° and 40° to the vertical is higher than under pure vertical loading due to coupling effects. Current practice assumes a reduced capacity leading to unnecessary over conservatism. In the demonstration exercise, this finding results in an increase of pile capacity by about 12%.

2. About this report

2.1. Introduction

Despite the COVID-19 world pandemic, the world's demand for energy continues to increase. By 2023, global demand for energy is forecast to reach its 2019 level and is expected to reach 740 million terajoules by 2040, corresponding to a 30% increase (World Energy Outlook 2020, iea.org). To limit global warming to 1.5 degrees Celsius, as set by the 2021 Paris Agreement, it is imperative that the majority of this increase is met by renewable energy. In Australia, the Renewable Energy Target is a legislated Australian Government scheme that operates until 2030, with a goal to achieve 33,000 gigawatt hours of additional renewable electricity from 2020 to 2030 (Australian Government, 23 June 2015).

Oceans cover 75% of the globe and the waves that propagate across their surface represent an energy-dense and reliable form of renewable energy. In the deep ocean, waves can travel remotely out of storm areas with minimal loss of energy, and progressively develop into regular, smooth waves or 'swell' that can persist for great distances (i.e. thousands of kilometres) from their origin. Figure 2.1 shows the distribution of world-wide wave power resources, where red zones represent the highest level of wave energy. The total potential of wave energy has been estimated to be 2 TW, which if harnessed, would be enough to supply the world's energy needs (Bhuyan, 2008). Australia in particular is well-placed to benefit substantially from wave energy given its proximity to the energy-rich Southern Ocean. According to the Australian Wave Energy Atlas (Hemer et al., 2018a), wave energy could contribute up to 11 per cent of Australia's energy demand (enough to power a city the size of Melbourne) by 2050, making it a strong contender in Australia's renewable energy mix.

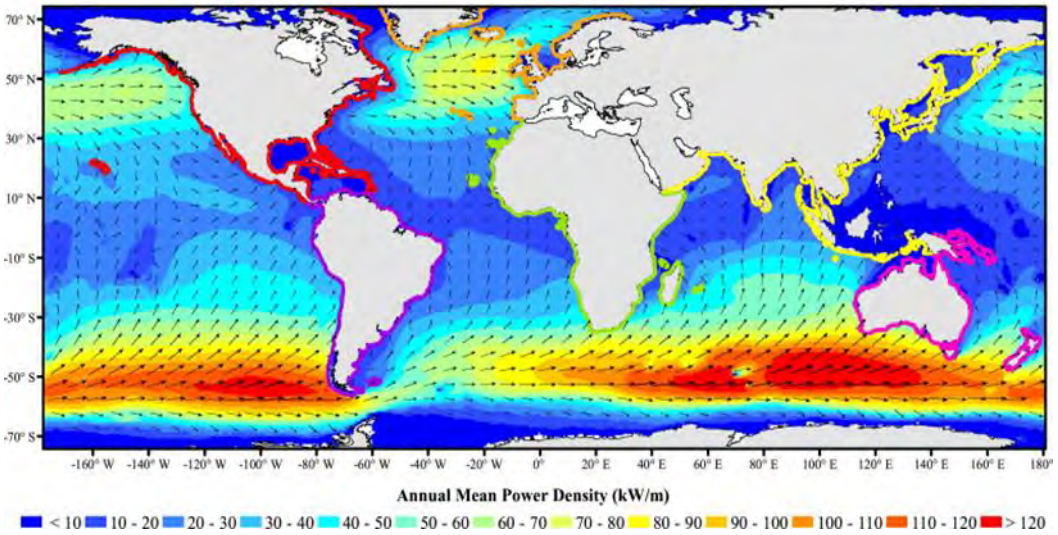

Figure 2.1. Global annual mean power density and direction (vectors) from Gunn and Stock-Williams (2012).

Despite its considerable potential, wave energy has not yet reached full commercial development. The cost of wave energy remains significantly higher than competing alternatives, including other sources of renewable energy such as wind or tidal power. This is principally due to the engineering challenges associated with installing and operating infrastructures in the ocean

environment. However, compared with – for instance wind energy – wave energy is an infant industry. Confidence that cost reduction can be achieved over time may be drawn by noting that over two decades ago the cost of wind energy was three to five times higher than the cost of conventional energy from fossil fuel, compared with only about one and a half times (or parity) today. This significant cost reduction reflects the technical developments and optimisations that have taken place in the intervening years and has allowed for the emergence of a global industry, particularly in European countries, where 15% of the electricity production was generated from wind in 2020 (Statista, 2021).

Currently, the cost of wave-generated electricity remains difficult to evaluate due to the lack of full-scale developments but can be estimated as being between two and three times the cost of fossil-fuel derived electricity, which reflects the development status of the wave energy industry (Hemer et al, 2018b). However, significant cost reduction opportunities are possible. For instance, mooring and anchoring can account for up to 30% of the overall development cost. Similarly, current installations of single wave energy device prototypes have not investigated potential efficiencies of scale, which would result from the development of arrays of multiple wave energy converters (WECs). An array of 100 WECs would occupy a large seabed footprint of about 2×2 km. This would increase the potential for spatial variability of geotechnical seabed properties and wave properties (that govern the loads applied to the foundations), which in turn would affect the reliability of the foundations unless significant conservatism is adopted in the foundation design.

While all these factors contribute significantly to the cost of wave energy, they can be mitigated by appropriate considerations associated with array configuration and location, better consideration of the spatial variability of the soil characteristics and of the specific nature of the loading generated by WECs on foundations, as addressed in this report. In particular, foundation design for offshore renewable energy devices has been adopted directly from the offshore oil and gas industry, with no consideration of the different economic, societal, and technical conditions. For instance, the foundation costs for an oil and gas facility are typically a mere 2% of the total installed costs (Moura Parades et al., 2013), such that the incentive to reduce conservatism in the foundation design is very low. The foundations and moorings for oil and gas facilities have a key role in (i) keeping a far larger proportion of the capital expenditure safely in position, (ii) avoiding environmental consequences of hydrocarbon fluid spills from ruptured pipelines, and (iii) ensuring the health and safety of persons on board the facilities. Furthermore, as most WECs are inherently designed to move unimpeded with the motion of the wave, the characteristics and variability of the loads on the foundation are likely to be different to those on a tautly moored floating hydrocarbon platform. Paradigm shifts away from the traditional approaches developed for the oil and gas industry are required, to reduce the installed costs of wave energy, so that widespread deployment of WECs on a commercial scale becomes viable.

Moreover, current practice for selecting new commercial WEC projects is often initially weighted heavily to identifying sites based on having ideal regional offshore (deep water) wave conditions to maximise wave generation capacity. Engineering solutions are then developed at largely pre-determined sites with subsequent consideration for economic viability only after the full costs are assessed. In order to reduce the cost of wave energy projects, there is a critical need to rethink this process by developing a comprehensive new knowledge framework that simultaneously considers how placement of WECs can be used to optimally balance both enhanced power generation and reduced total project costs (given that the latter is equally dictated by location,

which affects submarine cable distances, foundation requirements, etc.). This report presents such a framework, through a comparative exercise using the virtual deployment of a CETO 6 wave energy converter developed by Carnegie Clean Energy in Torbay, near Albany, Western Australia (WA).

2.2. Project scope

This project is a collaboration between the Wave Energy Research Centre at the University of Western Australia and Carnegie Clean Energy. It aims at reducing the cost of WECs by providing the scientific knowledge and engineering tools to build arrays of multiple WECs and to optimise their location and configuration in order to maximise power generation and minimise initial construction costs.

This was achieved by developing a cross-disciplinary and integrated approach that evaluates the combined influence of wave properties, seabed bathymetry and geotechnical characteristics to define the optimal location and arrangement of an array of twenty WECs that minimises the cost of installation and infrastructure while maximising the power output.

Specifically, the approach realises cost savings for commercial deployment of wave energy devices in large integrated arrays by providing innovation on four different aspects:

1. Developing a tool that optimises the location and arrangement of arrays of WECs as a function of mean power generation length of transmission cables connecting each WEC in the array to a sub-station and to the cable shore crossing, and coastal impact.
2. Characterising soil variability and its influence on foundation design in order to develop a methodology that establishes the appropriate level of soil characterisation and design conservatism (i.e. selection of appropriate design parameters) to minimise foundation cost.
3. Develop a new understanding of foundation performance under the specific loading regime generated by wave energy converters in order to establish optimised foundation design methods and reduce conservatism.
4. Combine the three elements described above into a methodical and rigorous approach in order to identify the best (optimum) location and arrangement of a WEC array that will minimise the ratio of cost to mean power output.

2.3. Reported outcomes

This report presents the integrated approach being developed, and its implementation on the virtual deployment of an array of twenty CETO 6 WECs in Torbay, near Albany, WA. The outcome is a comparison of the ratio of total cabling and foundation infrastructure cost to the mean power output (in $/MW) between a base case using standard industry practices and an optimised case using the outcomes of the research undertaken during this programme.

The exercise demonstrates a reduction of the normalised cost of cabling and foundation infrastructure to mean power output by ~23% resulting from careful consideration of the wave resource, bathymetry, soil variability and optimised design methods.

3. Methodology

3.1. Overview

The methodology used to demonstrate the cost saving achieved by using the integrated approach developed in this programme comprises a comparison of a base case deployment, with an optimised deployment that considers infrastructure cost (including cabling and foundations) and optimised design procedures that better account for soil variability and loading characteristics.

Specifically, the base case assumes that the location for deployment is identified based on expected maximum power output only, irrespective of other considerations such as soil characteristics, foundation engineering and cabling costs.

In the optimised case, two phases are considered. The first phase aims to identify the best (optimal) location among nine separate options considering both power output and infrastructure cost, including cabling, site characterisation and foundation engineering. In the second phase, an additional optimisation at the location identified in Phase 1 is undertaken by establishing the ideal array geometry and optimising the foundation design by considering soil variability and improved design methods accounting for the specific loading characteristics generated by the CETO 6 device.

In detail, the process followed the steps outlined below:

Base case

1. Select the array arrangement.
2. Identify the preferred location for deployment in Torbay.
3. Calculate the mean power output.
4. Calculate the foundation design loads.
5. Establish the characteristics of the seabed at the selected location.
6. Design the foundation based on minimal site characterisation and standard design methodologies.
7. Calculate the overall cost of deployment including cabling, site characterisation, and foundation installation.
8. Calculate the ratio of mean power output to total cost (to be used as a comparison metric).

Optimised case - Phase 1: Identify optimal location

1. Select nine separate possible array-centre locations in Torbay.
2. Calculate the mean power output at the nine locations.
3. Calculate the foundation design loads at the nine locations.
4. Establish the seabed characteristics at the nine locations.
5. Design the foundation based on minimal site characterisation and standard design methodologies.
6. Calculate the overall cost of deployment including cabling, site characterisation, and foundation installation for the nine locations.

7. Calculate the ratio of cost to mean power output for the nine locations.
8. Identify the optimal location yielding the lowest cost to power ratio.

Optimised case - Phase 2: Optimise arrangement and foundation design

1. Optimise the array configuration at the optimal location in order to maximise power output and minimise cable distance (using multi-objective optimisation).
2. Estimate coastal impacts for the optimised configuration (from step 1) to further optimise the array with minimal coastal impact.
3. Calculate the foundation design loads for the new array configuration.
4. Establish the soil characteristics using an optimised approach.
5. Design the foundation using an optimised design method.
6. Calculate the overall cost of deployment at the optimal location.
7. Calculate the ratio of cost to mean power output and compare this to the base case to establish the cost reduction.

3.2. Assumptions and variables investigated

Several assumptions were made to undertake the comparative exercise. These assumptions were inherent to the location of the virtual deployment and were necessary in order to compensate for the lack of data and to simply the problem, which is extremely complex when considering the total number of variables. The following assumptions were made:

- The wave regime in Torbay has been characterised by Cuttler et al. (2020) from measurements gathered by the Wave Energy Research Centre.
- The wave energy converter is a CETO 6 device, developed by Carnegie Wave Energy. The CETO 6 has three taut mooring lines, each connected to a separate foundation.
- An array of twenty WECs has been chosen as a reasonable development size for potential connection to the electricity grid (corresponding to a 20 MW development for a CETO 6 array).
- The bathymetry has been established by a multi-beam bathymetric survey and an aerial lidar survey.
- Without a geotechnical site investigation campaign, the seabed conditions are assumed to consist of a single unit (layer) of sand as commonly found in water depth 0-200 m.
- The relative density of the sand is considered to vary from 60 to 85% as a function of the water depth, with local variability determined by random theory.
- The foundation type selected is driven steel tubular piles (of 4 m diameter and wall thickness 50 mm).
- The array is connected to a grid connection point located at coordinates 571469.26 E 6120111.5 N (UTM zone 50S).
- The costing model is based on standard cost estimate values found in the literature.
- The optimisation analysis considered the following parameters:
    - The wave characteristics and the associated mean power within Torbay.
    - The bathymetry within Torbay.
    - The length of cables within the array and from the array to the grid connection point.
    - The relative density of the sand constituting the seabed.

- The variability of the sand relative density and the resulting pile length necessary to resist the mooring loads.
- The coastal impact of the array characterised by the maximum alongshore sediment transport gradient.

It should be noted that other parameters could have been considered in the optimisation (e.g. location of the grid connection point, cost of specific items, type of foundations, etc.) These parameters were not considered because either they would unnecessarily complicate the analysis or insufficient information was available to consider them meaningfully. While these parameters would indeed affect the outcome of the analysis with respect of the total saving achieved, it is believed their omission would not adversely affect the outcome of the optimisation approach.

3.3. Limitation of the project

The project is limited to the wave characteristics at Torbay, and the specificities of the site and wave energy converter considered. While the approach can be generalised and used for any type of wave energy converter deployment in any location, the exact cost reduction expected will depend on multiple parameters including those not investigated in this project.

3.4. The Torbay site

Torbay is a south-west facing semi-enclosed embayment that is directly exposed to incident wave energy from the Southern Ocean (SO). Cuttler et al. (2020) conducted a comprehensive wave resource assessment for the site and found an annual average wave resource of 47 kW/m with seasonally averaged significant wave heights ranging from 2.15 m (30 kW/m) in the summer to nearly 3 m (65 kW/m) in the winter.

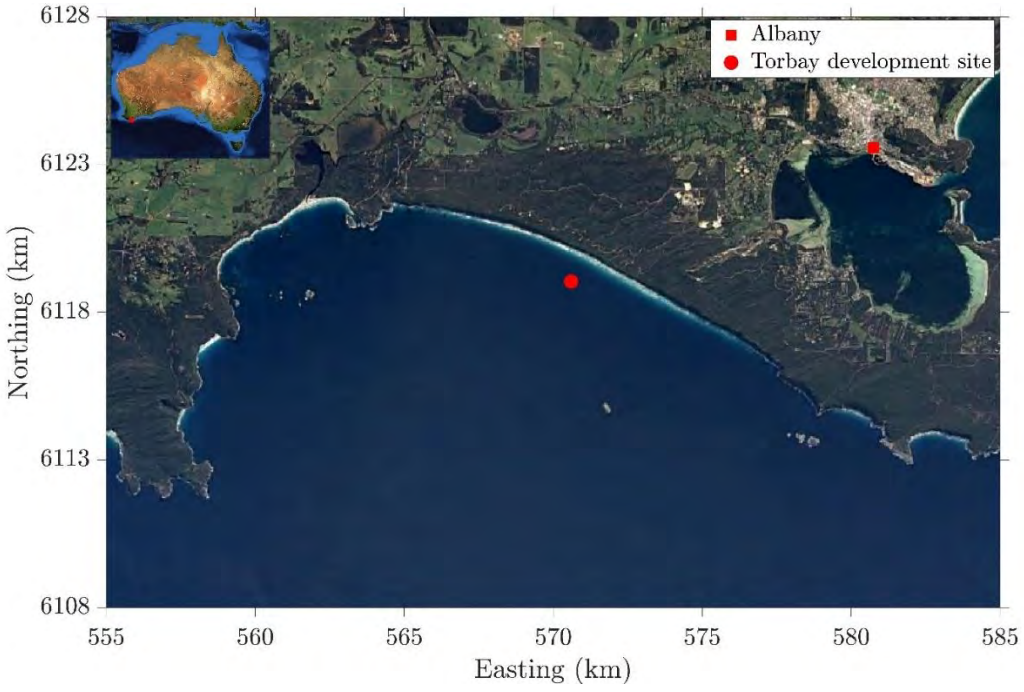

Figure 3.1. The Torbay development site in Western Australia.

The mean period and direction variability is also limited with seasonally averaged variability in mean direction less than 10 degrees and less than 2 s for mean period. The exposure to consistent swell from the SO coupled with the relatively small range in seasonal wave energy variability makes Torbay and ideal wave energy development site. Torbay is also directly offshore of an existing terrestrial wind farm that includes electrical grid infrastructure directly onshore. The coastline is composed of a steep bluff (~50 m high) and a beach that is primarily composed of a limestone platform that is seasonally covered with sand. The seabed offshore in depths >10 m is gradually sloping with the exception of rock outcrops including Stony Island on the south-east side of Torbay (Figure 3.1).

3.5. The CETO 6 wave energy converter

The CETO 6 device is a point absorber wave energy converter developed by Carnegie Clean Energy over the last 15 years (Figure 3.2). Being a submerged and close to the surface device, it reduces the natural frequency without increasing the volume or adding another oscillating body as the hydrostatic stiffness becomes null when the device is submerged. This translates in the device easily resonating with the incoming ocean waves frequency and increasing its power to weight ratio. Considering that heave is not the only dominant direction of the wave excitation forces as the device is submerged and the wave excitation forces in the other directions become more prominent (Sergiienko and al, 2017), CETO 6 is designed to capture energy from all the wave excitation forces' directions. Therefore, by tuning the device properly to take advantage of most of the dominant wave excitation forces, it can capture more energy than heaving point absorbers. Another advantage that CETO features being completely submerged is that it does not require a locking mechanism to lock the device in the events of a storm or extreme waves as it is protected from the elements by being underwater.

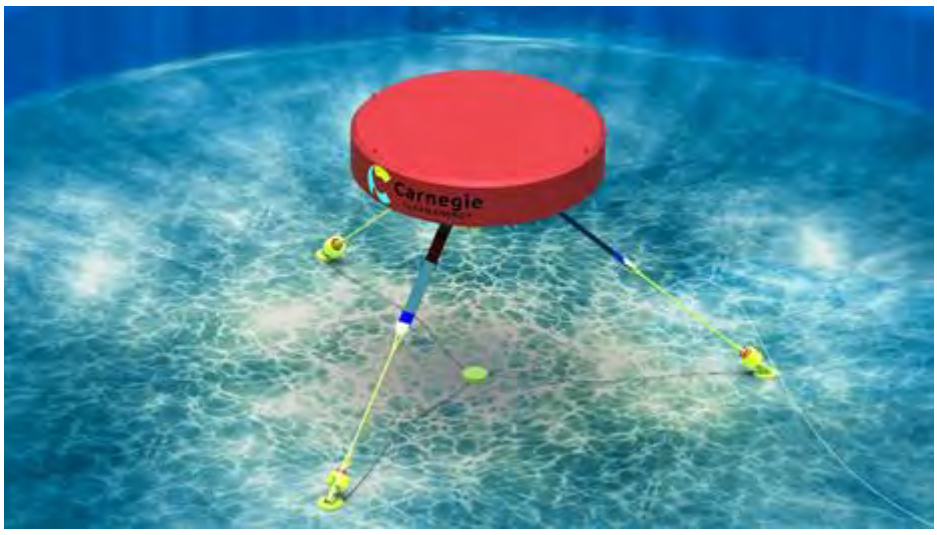

Figure 3.2. Carnegie CETO 6 device.

CETO 6 includes three power take off (PTO). The PTO transforms the kinetic energy captured from ocean waves into electrical energy and constitutes one of the most fundamental parts of WECs (Falcão, 2010) and a large part of the cost of the device. Some point absorbers use magnetic direct drive linear generators mainly to reduce the complexity of the system they do not require a mechanical interface to transmit the mode of motion (Ulvgård et al. 2016). Even though the use of direct drive linear generators is interesting for offshore applications, the prohibitive costs of

manufacturing and the challenges associated with the use of magnets have pushed the industry towards rotary motion transfer mechanisms with the inclusion of rotary generators to generate the power (Rhinefrank et al, 2012, Al Shami et al. 2018). Unlike typical point absorbers, CETO utilises rotary electric PTOs to transform kinetic energy from ocean waves into electric energy with innovative methods to capture the energy from the different modes of motions.

4. Base case analysis

4.1. Location and array configuration

The base case comprises an array of twenty WECs assembled in two rows of ten, along the 30 m water depth line (the optimum water depth to deploy the CETO 6) at the location L3 directly in front of the grid connection point (See Figure 4.1 and Figure 4.2). The twenty-WEC farms were arranged in two rows with a constant inter-WEC spacing of 150 m (the minimum spacing to prevent WEC collisions and allow vessel access to each WEC). The row spacing is the same as the inter-WEC spacing. The location was selected based on preliminary assessment of the wave conditions, its geographical location and water depth.

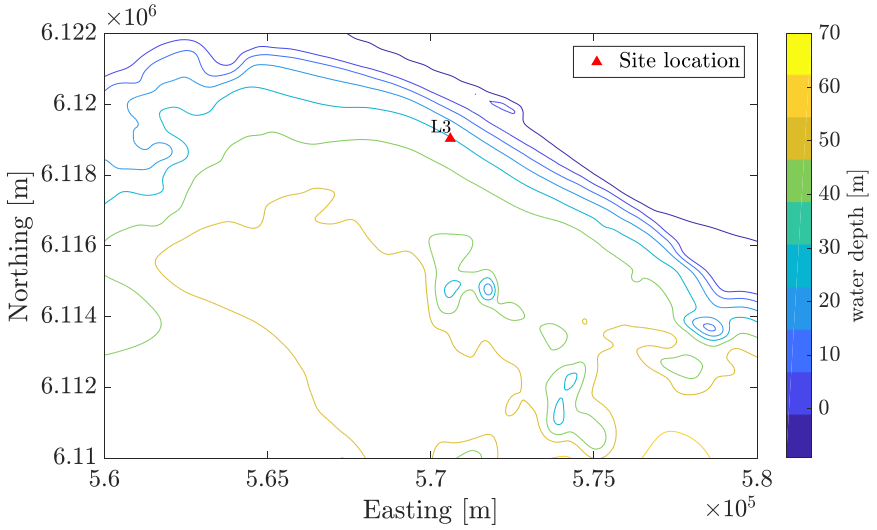

Figure 4.1. Torbay, Albany site in Western Australia. Markers indicate the considered location for base case.

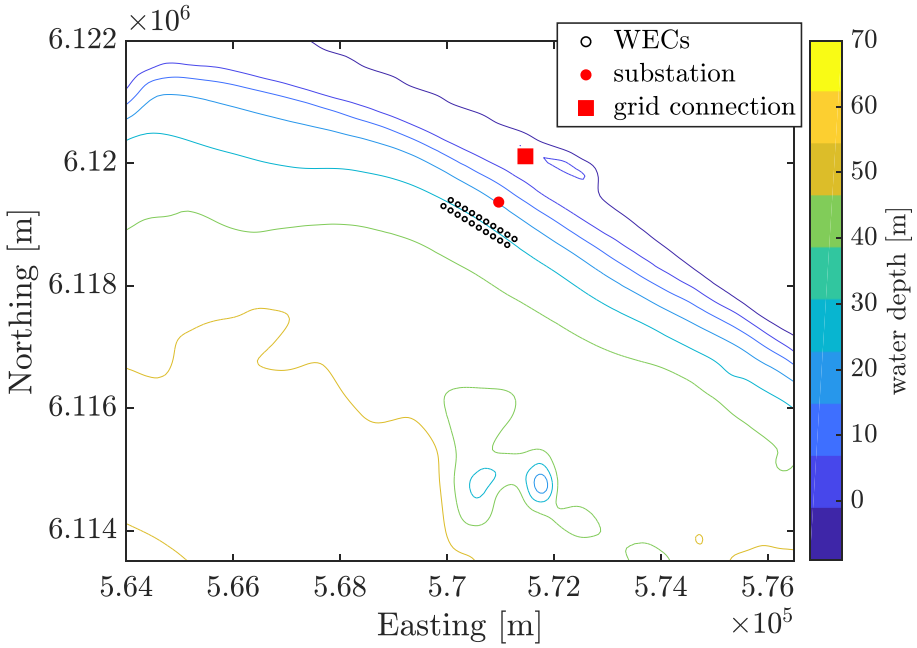

Figure 4.2. Wave farms location and arrangement for the base case.

4.2. CETO 6 configuration

The geometric parameters of the WEC, e.g., diameter and height of the buoyant actuator (BA) were kept constant throughout the study as 25 m and 5 m, respectively. The device was moored to the seabed at 30 m water depth (for L3) and the BA submergence depth was fixed at 2 m (see Figure 4.3). The BA is moored using three flexible tethers connected to distinct power take-offs (PTOs) allowing power generation from multiple modes of motion.

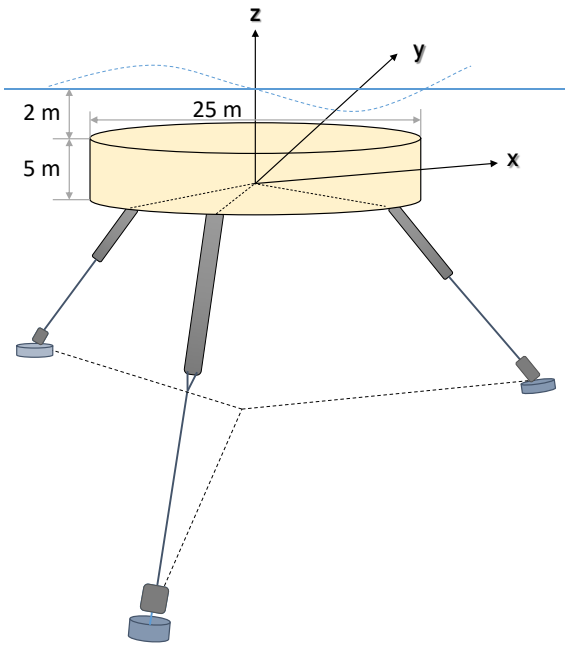

Figure 4.3. Sketch of the shallowly submerged cylindrical point absorber with three taut tethers.

4.3. Power estimation

The total mean power produced by an array of twenty WECs oscillating in six degrees of freedom, under the assumption of linear wave theory, is calculated based on Budal (1977), Thomas et al. (1981) and Falnes et al. (1982) as:

$$P = \frac{1}{4}\left[\hat{U}^{*}\hat{F}_e + \hat{F}_e^{*}\hat{U}\right] - \frac{1}{2}\left[\hat{U}^{*}B\hat{U}\right] \qquad \textit{Eq. 1}$$

where $\hat{U}$ is the vector of complex velocity amplitudes, $\hat{F}_e$ is the vector of complex excitation forces (including array interactions), B is the matrix of radiation damping coefficients and the asterisk in the superscript implies the complex conjugate transpose. The $\hat{U}$ is obtained based on frequency domain solutions to the linear equation of motions given by Falnes (2002),

$$\hat{F}_e(\omega) = \left[i\omega(M + A_m) + \left(B + B_{pto}\right) + \frac{K_{pto}}{i\omega}\right]\hat{U}(\omega) \qquad \textit{Eq. 2}$$

where $A_m(\omega)$ and $B(\omega)$ are the frequency-dependent added mass and radiation damping matrices respectively, M is the mass matrix, K_{pto} and B_{pto} are the linearised PTO spring and damping coefficient matrices respectively (see Orszaghova et al. (2020) for more details); the PTO coefficients are assumed identical for all three PTOs (in the three tethers). Each WEC can move in all 6 degrees of freedom (surge, sway, heave, roll, pitch and yaw); however, in the linearised

system, all modes apart from yaw contribute to power production (Orszaghova et al., 2020). The hydrodynamic coefficients are obtained from the linear potential flow model of McCauley et al. (2018) which also accounts for array interactions. For the fully submerged device, the hydrostatic stiffness is zero and the restoring force is achieved mechanically through the PTO. Apart from the placement of each WEC in the array, the PTO coefficients are another set of design variables to be optimised. In this study, for a given array, the PTO coefficients are kept constant for all sea states but optimised to maximise the mean power output from the wave climates. To optimise the PTO coefficients in the present work, we utilised the MATLAB in-built global optimization toolbox (The Mathworks, Inc. MATLAB, Version 9.6, 2019). The range of coefficients was restricted based on initial trials as:

$$\begin{cases} 10^6 \leq k_{pto,i} \leq 10^7\ N/m \\ 10^6 \leq b_{pto,i} \leq 10^7\ N/(m/s) \end{cases} \qquad \forall i = 1, 2, \ldots, 20. \qquad \text{Eq. 3}$$

The imposed range of k_{pto} and b_{pto} was found to be sufficient, as the optimised coefficients were found to be well within the lower and upper bounds. Details regarding the PTO coefficients validation can be found in the attached paper (David et al. 2021).

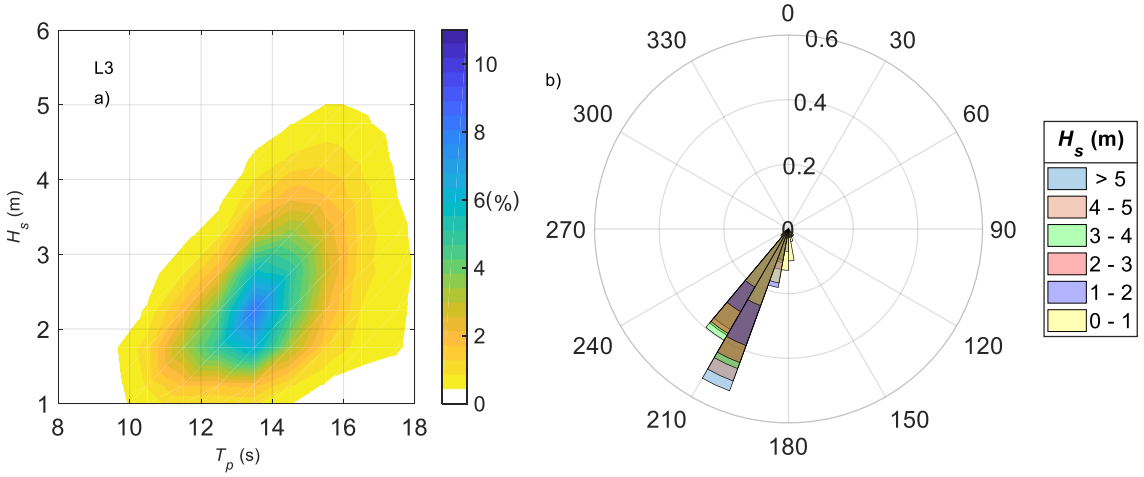

Figure 4.4. L3 wave climate at Torbay, Albany site in Western Australia. The joint occurrence distributions of significant wave height H_s and (a) peak wave period T_p; (b) and mean wave direction β_m (°).

We used numerically simulated wave data from Torbay near Albany in Western Australia as the input wave climate (Cuttler et al., 2020). For illustrative purposes, the wave conditions at L3 are shown in Figure 4.4. For more details on the seasonal and interannual variability of the site's wave climate, refer to Cuttler et al. (2020). The mean power generation was calculated as:

$$P_{mean} = \sum_{l=1}^{L} \left(P_l(H_s, T_p, \beta_m) O_l(H_s, T_p, \beta_m) \right) \qquad \text{Eq. 4}$$

where H_s, T_p, and b_m are the significant wave height, peak wave period and mean wave direction respectively. L represents the total number of sea states considered, O_l represents the probability of occurrence of the l^{th} sea state and Pl represents the power absorbed in the l^{th} sea state:

$$P_l = \int_0^\infty 2S_l(\beta_{m,l},\omega)\frac{P}{A^2}(\beta_{m,l},\omega)d\omega \qquad \text{Eq. 5}$$

where A is the incident wave amplitude, S_l is the power spectral density of the l^{th} sea state, here defined by a JONSWAP spectrum with peak enhancement factor $\gamma = 3.3$. In this report, we focused only on long-crested waves because the directional spreading at the development site is rather low (mean peak directional spreading of 17.5°). Based on this methodology and the array parameters and wave climate the mean power absorbed by the wave farm at site L3 was calculated as 9.13 MW.

4.4. Foundation engineering

For the base case, the foundations for the two-row WEC devices at location L3 (water depth h = 30 m) were designed based on the site-specific load distribution and a minimum-scope site investigation (SI) that includes a single cone penetration test (CPT) at the centre of the site (see Figure 4.5).

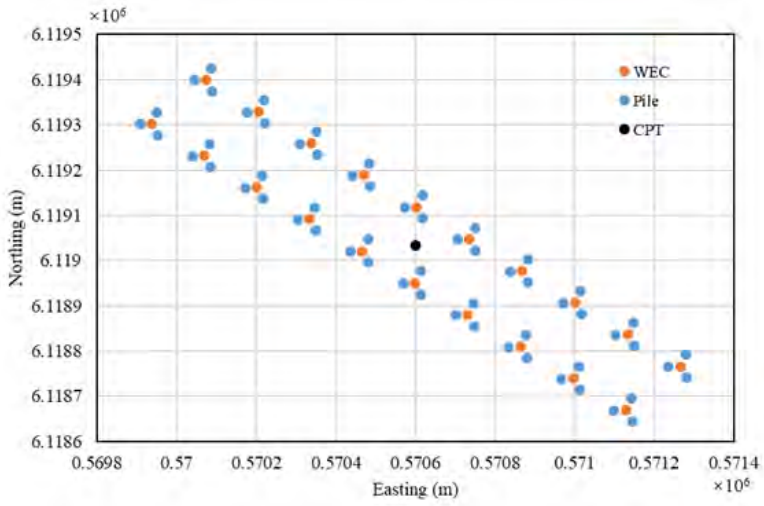

Figure 4.5. Locations of WECS, piles and CPT for the base case (location L3).

4.4.1. Site conditions

Load distribution

The piles were designed using the short-term load S (duration time = 3 hours). The short-term empirical cumulative distribution function $G_S(s)$ of load for this site was calculated using linear wave/structure interaction theory (Faltinsen, 1990). $G_S(s)$ is expressed as:

$$G_S(s) = P(S \leq s) \qquad \text{Eq. 6}$$

where $P(S \leq s)$ is the probability that the observed short-term load S does not exceed the load threshold s.

To calculate the load on each foundation, we first calculated the vertical load transfer function, $F_{l,n}$ (n = 1,2,3), considering linear spring and damping forces as:

$$F_{l,n} = \left(k_{pto}\Delta L_n + b_{pto}\dot{\Delta L_n}\right)\frac{T_n}{|T_n|}.\hat{k} \qquad \textit{Eq. 7}$$

where T_n is the instantaneous tether vector from the attachment point to the seabed and $\hat{k}$ is the unit vector. ΔL_n and $\dot{\Delta L_n}$ are the change in tether length and the rate of change in tether length respectively, both of which are a function of the displacements of the body. K_{pto} and b_{pto} are the stiffness and damping coefficients respectively. Once the F_l was obtained, the variance of the load σ_r^2 for different sea states was calculated from:

$$\sigma_r^2 = \int_0^\infty S_l(\omega)\left|\frac{F_l}{A}(w)\right|^2 d\omega \qquad \textit{Eq. 8}$$

We assumed that the load amplitudes follow the Rayleigh distribution (like the wave amplitudes). The short-term load was then calculated as:

$$R_{max} = \sqrt{2\sigma_r^2 log\left(\frac{t_s}{T_p}\right)} \qquad \textit{Eq. 9}$$

where t_s is the short time and T_p is the peak wave period. The static pre-tension force, which is a function only of net buoyancy, was then added. The resulting $G_S(s)$ is shown in Figure 4.6.

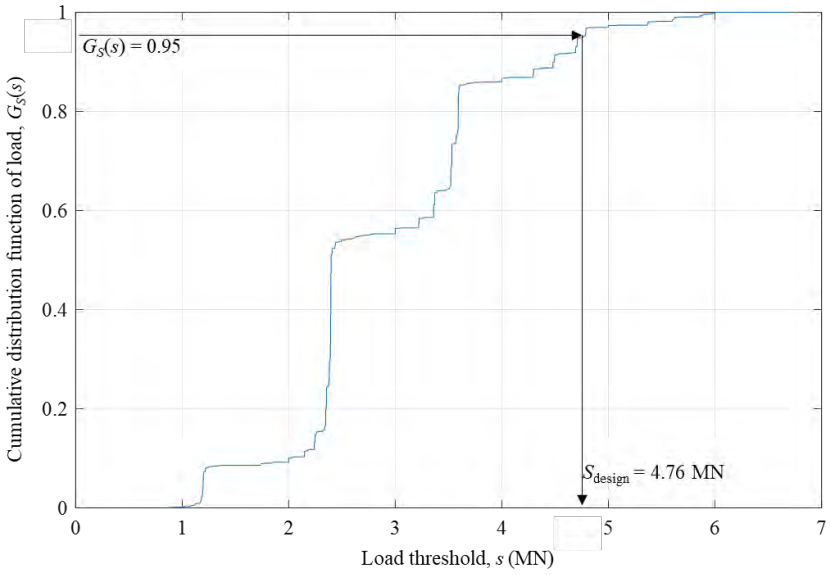

Figure 4.6. Empirical load cumulative distribution function for the base case (location L3).

Cone penetration test data simulation

In the absence of site characterisation at Torbay, we created a virtual seabed with characteristics relevant to the geology of the site. For the base case a single set of cone penetration resistance (q_c) data was simulated using random field theory (Vanmarcke, 2010) to account for natural variability, and expressed in terms of the superposition of a depth-wise trend (μ_{qc}) and a residual variation. We defined the depth-wise trend of q_c using the following equations (Lunne et al., 1997):

$$D_r = \frac{1}{2.61} ln\left[\frac{\mu_{qc}}{181(\gamma_{sat}-\gamma_w)z^{0.55}}\right] \qquad \textit{Eq. 10}$$

$$D_r = \frac{e_{max} - e}{e_{max} - e_{min}}$$ *Eq. 11*

$$\gamma_{sat} = \frac{\gamma_s - e\gamma_w}{1+e}$$ *Eq. 12*

where D_r is the relative density of soil; γ_{sat}, γ_w (= 9.8 kN/m3) and γ_s (= 26.5 kN/m3) are the unit weight of saturated sand, water and soil grains, respectively; e, e_{max} (= 0.8) and e_{min} (= 0.4) are the natural, maximum and minimum void ratio; z is the depth below the mudline of the seabed.

According to the free fall penetration tests conducted by Stark et al. (2019) across and along the sandy nearshore zone of Phipps Peninsula in Yakutat, Alaska, the mean relative density (D_r) for offshore sandy soil can exhibit an exponential decreasing trend with the increase of water depth h (Figure 4.7). In this work, we assumed the seabed to be constituted of dense sand, and we defined the variation of mean D_r as a function of water depth:

$$D_r = 0.35exp\left(-\frac{h}{38}\right)^5 + 0.6$$ *Eq. 13*

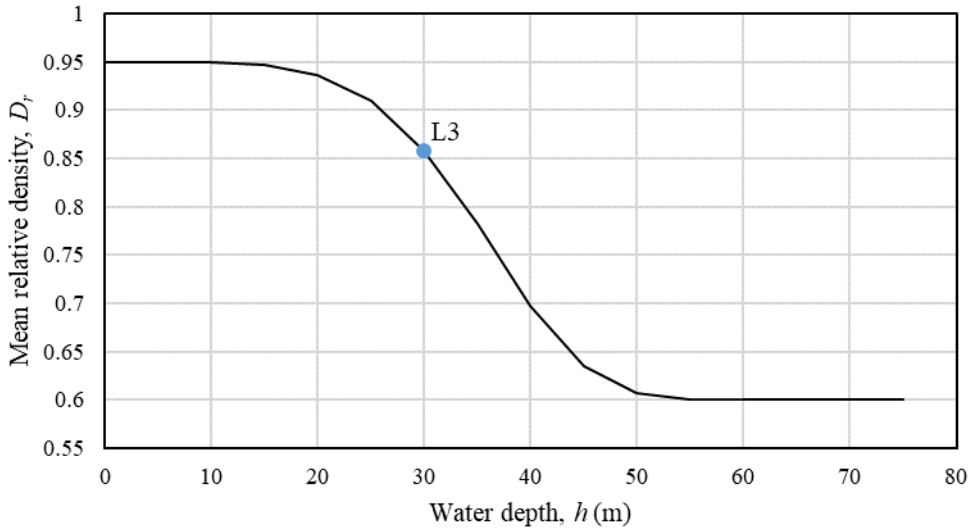

Figure 4.7. Mean relative density for soils at different water depth

Based on Eq. 13, the mean D_r for the seabed at location L3 (h = 30 m) is 85.8% as shown in Figure 4.7. Note that the mean D_r was assumed to be independent of depth below mudline (z).

The residual variation of q_c can be conveniently described by a coefficient of variation of q_c ($\mathrm{COV}(q_c)$) and an autocorrelation function. The $\mathrm{COV}(\cdot)$ is defined as the ratio between the standard deviation and the mean of the samples. An exponential autocorrelation function $\rho(\cdot)$ was chosen to characterise the spatial correlation of the q_c residuals (Baecher & Christian, 2003):

$$\rho(\tau_{ij,h}, \tau_{ij,v}) = exp\left[-2\left(\frac{\tau_{ij,h}}{\theta_v} + \frac{\tau_{ij,v}}{\theta_v}\right)\right]$$ *Eq. 14*

Where $\tau_{ij,h}$ and $\tau_{ij,v}$ are the distance between spatial points i and j in the vertical direction; θ_h and θ_v are the scales of fluctuation in the horizontal and vertical directions, respectively. The exponential autocorrelation function was adopted because it is the most commonly used autocorrelation function form (e.g. Zhu and Zhang, 2013; Li et al., 2015). Values of COV(q_c)= 0.3,

θ_h = 40 m, θ_v = 1.5 m were adopted in the following simulation, because they are within the ranges of the frequently observed values (Phoon & Kulhawy, 1999; Uzielli et al., 2019). Based on Eqs. 10 to 14, the q_c values at different spatial points of the seabed can be simulated as a lognormal random field. In this work, the random field was generated using the Karhunen-Loeve (KL) expansion method (Schwab & Todor, 2006). The KL expansion method is based on the covariance kernel modal decomposition on a finite domain. Compared to other random field generation methods, such as local average subdivision method (Vanmarcke, 2010), the turning band method (Mantoglou & Wilson, 1982), and midpoint method (Der Kiureghian & Ke, 1988), KL expansion generally requires the fewest random samples for a prescribed level of accuracy. Based on KL expansion, the q_c value at location (x, y, z) ($q_c(x, y, z)$) can be expressed as:

$$q_c(x,y,z) = exp\left[\mu_{qc,ln}(x,y,z) + \sum_{i=1}^{M} \sigma_{qc,ln}(x,y,z)\sqrt{\lambda_i} f_i(x,y,z)\xi_i\right], (x,y,z) \in \Omega \qquad \textit{Eq. 15}$$

where $\mu_{qc,\ln}(\cdot)$ and $\sigma_{qc,\ln}(\cdot)$ are the mean and standard deviation of logarithm q_c, respectively; λ_i and $f_i(\cdot)$ are the i^{th} largest eigenvalue and the corresponding eigenfunction of the autocorrelation function, respectively; ξ_i is the i^{th} independent standard normal random sample; M represents the truncation terms of the KL expansion; Ω is the soil domain. Based on Eq. 15, the q_c values for different spatial points of the seabed were simulated. The simulated q_c profile at the measured location (the black dot shown in Figure 4.5) extracted from the random field is shown in Figure 4.8.

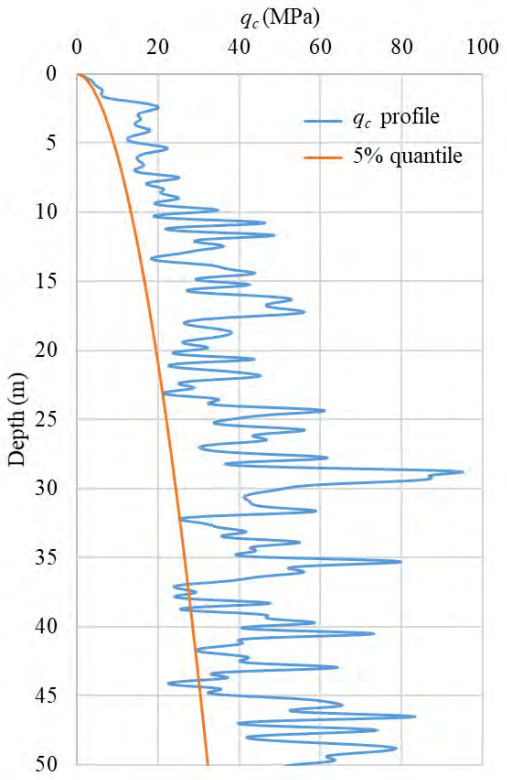

Figure 4.8. Virtual CPT data and the 5% quantile of qc for the base case (location L3).

4.4.2. Pile design

The pile sizing procedure was undertaken using the ISO (2020) partial load and material factor (or LRFD) approach as developed below.

Number and locations of piles

For each WEC, three piles were used to anchor the device (sixty piles in total). The angle between adjacent mooring lines is 120°. The orientations of the three piles are the same for the twenty WECs so that in the wave farm a four-row pile layout (Figure 4.5) was obtained.

Design load

The unfactored design load S_{design} was determined from the 95% quantile of load distribution, i.e. $G_S(S_{\text{design}}) = 0.95$. As shown in Figure 4.6, $G_S(S_{\text{design}}) = 0.95$ corresponds to an $S_{\text{design}} = 4.76$ MN. Based on ISO (2020), the S_{design} was multiplied by a load factor $\gamma_L = 1.35$ (i.e. $\gamma_L S_{design} = 1.35 \times 4.76 = 6.43$ MN) which corresponds to a 'live' environmental load for the extreme design condition. Subsequently, the load was further divided by a factor $\gamma_{inc} = 0.8$ (i.e. $\gamma_L S_{design}/\gamma_{inc} = 1.35 \times 4.76/0.8 = 8.03$ MN) to account for the inclination of the applied load as the tether is inclined 40° from the vertical. Without any relevant information in the literature, this is a reasonably conservative assumption to account for the potential detrimental coupling between the vertical and horizontal components of the load (see Figure 5.21).

q_c design line

It is noted that there is no typical recommended sample quantile (SQ) of q_c (i.e. q_c(SQ)) for determining pile capacity in geotechnical engineering practice. For example, Eurocode 7 (BS EN 1997-1:2004) recommends the 5% quantile, while Japanese design codes for port facilities recommend a 30% quantile (Ching & Phoon, 2012). In this project, we selected the SQ = 5% of the unfactored q_c design line for pile sizing as recommended by Eurocode 7. This conservative approach is required in this case where limited information about the soil characteristics is available. The quantile regression method (Uzielli et al., 2019) was used to calculate the unfactored q_c(5%) (e.g. the orange curve shown on Figure 4.8). Subsequently, we divided q_c(5%) by a material factor $\gamma_m = 1.25$, i.e. $q_c(5\%)/\gamma_m$ as recommended by ISO (2020).

Pile sizing

We fixed the outer pile diameter *D* (= 4 m) and the pile wall thickness *t* (= 80 mm) so that only the pile length *L* was varied to fulfil the axial capacity requirements. We used the UWA-05 method (Lehane et al., 2005) to calculate the axial capacity R of the open-ended pile based on the constant volume interface friction angle (δ_f) and the $q_c(5\%)/\gamma_m$ data. We used a single deterministic value of $\delta_f = 29°$ as done in practice. The value of 29° was selected based on recommendations for offshore steel pile design (Liu et al., 2019) which in turn were based on a database of ring shear steel interface tests on sandy-silty soils. These tests showed low sensitivity of δ_f to fines contents, mineralogy, and normal stress level variations. The UWA-05 design equations (Lehane et al., 2005) are expressed as follows:

$$R\left[\frac{q_c(5\%)}{\gamma_m}\right] = \pi D \int_0^L \tau_f dz \qquad \textit{Eq. 16}$$

$$\tau_f = 0.0225 \frac{q_c(5\%)}{\gamma_m} tan\delta_f \left\{1 - min\left[1, \left(\frac{D}{1.5}\right)^{0.2}\right]\left(\frac{D_i}{D}\right)^2\right\}^{0.3} \left[max\left(\frac{H}{D}, 2\right)\right]^{-0.5} \qquad \textit{Eq. 17}$$

where τ_f is the local shaft friction; D_i is the inner diameter of the pile; H is the height above the pile tip.

The above pile sizing method is also summarised in Figure 4.9 and yielded a required pile length L = 18.2 m.

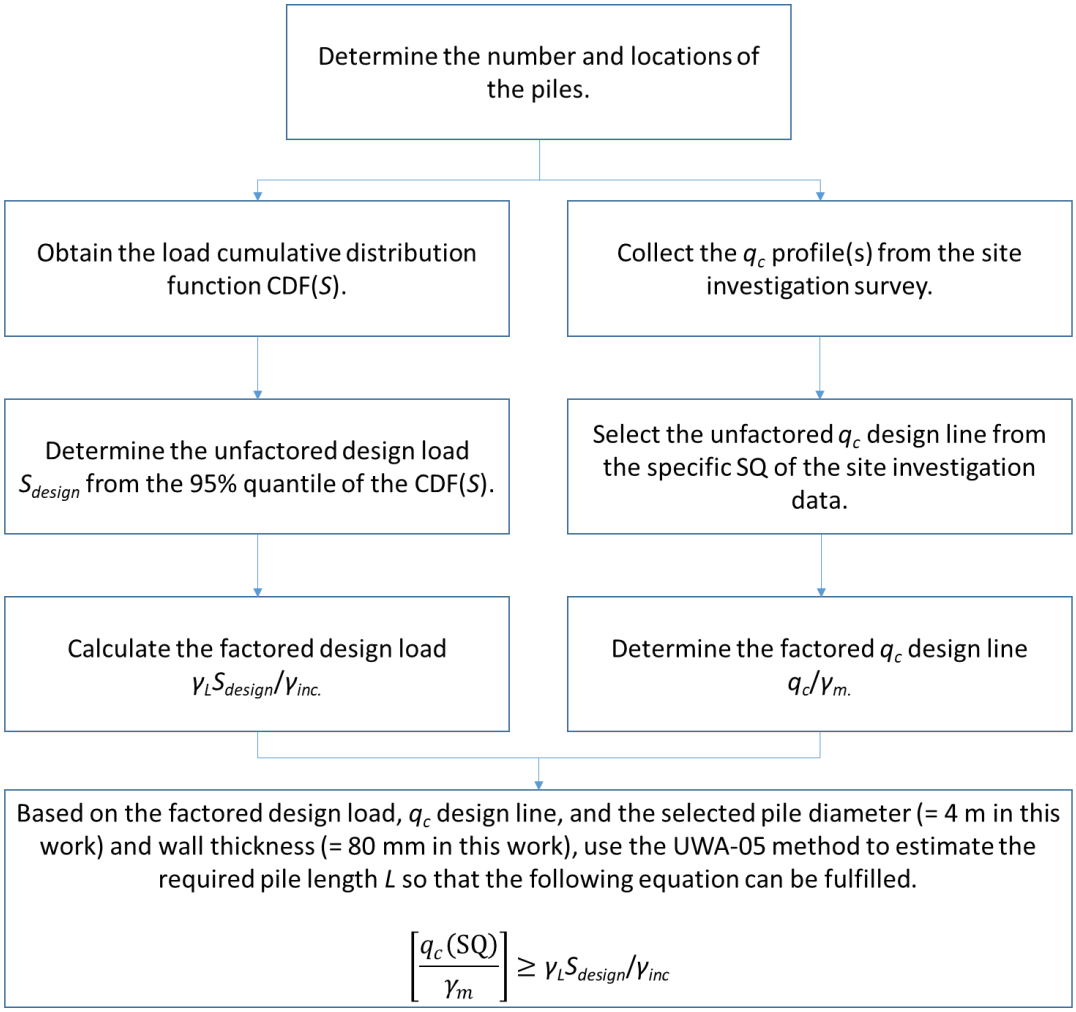

Figure 4.9. Summary of pile design procedure.

4.5. Costing

4.5.1. Cable cost

The cabling for the WECS array comprises three elements:

1. The dynamic cables from one WEC to the adjacent WEC within the array.
2. The subsea cable from the array to the substation.
3. The export cable from the substation to the grid connection.

The lengths of the different cable sections are presented in Table 4.1. For simplicity, it was assumed that the cost of cabling was \$400/m for the first element noted above and \$3,000/m for the second and third elements. This is considered to be a reasonable assumption for an export cable, noting that Horizontal Directional Drilling is likely to be used for the shore crossing (to the grid connection). This leads to a total cost of the cabling of \$5.3M.

Table 4.1. Length of cable for the base case in L3.

Site Locations	Within array (m)	Wave farm to substation (m)	Substation to the grid connection point (m)	Total (m)
L3	2838.1	497.3	898.7	4234

4.5.2. Foundation cost

The foundation cost consists of three components: (1) the geotechnical site investigation cost ($Cost_{GSI}$); (2) the pile fabrication cost ($Cost_{PF}$) and; (3) the pile installation cost ($Cost_{PI}$). The final pile cost is the sum of the three components.

Geotechnical site investigation cost

$$Cost_{GSI} = Cost_{VM} + Cost_{CPT} \times N_{CPT} \qquad \textit{Eq. 18}$$

where $Cost_{VM}$ (= \$500,000) is the vessel mobilisation cost; $Cost_{CPT}$ (= \$75,000/CPT) is the cost per CPT; N_{CPT} is the number of CPTs.

Pile fabrication cost

$$Cost_{PF} = \alpha_F \times Cost_{Steel} \times w_{Steel} \qquad \textit{Eq. 19}$$

where α_f (= 1.2) is the pile fabrication factor; $Cost_{Steel}$ (= \$3,500/tonne) is the steel unit cost; w_{Steel} is the total steel weight.

Pile installation cost

$$Cost_{PI} = Cost_{VesselM} \times T_{Mobilisation}(day) + Cost_{Install} \times N_{Pile} \qquad \textit{Eq. 20}$$

$$Cost_{Install} = Cost_{VesselO} \times T_{Install}\,(\text{day}) \times \alpha_I$$

$$T_{Install} = T_{PP}(\text{day}) + T_{PD}\,(\text{sec})/(3600 \times 24)$$

$$T_{PD} = N_{Blow} \times L \times T_{Hammer}(\text{sec/blow})$$

where $Cost_{VesselM}$ (= \$150,000/day) is the vessel mobilisation/demobilisation day rate; $T_{Mobilisation}$(= 28 day) is the mobilisation/demobilisation duration; $Cost_{Install}$ is the installation cost per pile; N_{Pile} is the number of piles; $Cost_{VesselO}$ ((= \$200,000/day) is the vessel operation day rate; $T_{Install}$ is the installation duration of each pile; $\alpha_I = 1.2$ is the installation downtime/contingency factor; T_{PP} (= 0.33 day) is the preparation duration for each pile; T_{PD} is the driving duration for each pile; N_{Blow} is the number of driving blows of each pile per metre penetration; L is the pile length; T_{Hammer} (= 6 sec/blow) is the hammer blow period.

As discussed in Section 4.4, we designed the sixty piles (with L = 18.2 m, D = 4 m, t = 80 mm) for the wave farm using a single CPT. By substituting these design parameters into Eq. 20, the foundation cost can be calculated. The details of the base case foundation cost estimation are listed in Table 4.2.

Table 4.2. Cost estimation for the base case (location L3).

Items	Values ($M)
$Cost_{GSI}$	0.575
$Cost_{PF}$	35.47
$Cost_{PI}$	16.28
Total foundation cost	52.325
Cable cost	5.323
Total cost	57.648

4.5.3. Total Cost

The total infrastructure cost (i.e. sum of the cable cost and foundation cost) for the base case is also presented in Table 4.2. In this work, the economic benefit of the optimised wave farm design was evaluated by the ratio of total cabling and foundation infrastructure cost to mean power output (denoted as the normalised cost). As discussed in Section 4.3, the mean power output for L3 is 9.13 MW, such that the normalised cost is $6.316M/MW.

Note that this is not a typical metric and can't be compared with capital cost figures used in other energy generation technologies. Additionally, this number does not include the capital cost associated with the WEC.

5. Optimisation analysis

5.1. Phase I: Optimal location

For the Phase I optimisation, we considered nine locations as shown in Figure 5.1. The locations L1 to L5 were fixed along the 30 m depth contour, while locations L6 to L9 were fixed in varying water depth from 35 m to 50 m and in line with L3 (in the alongshore position of the onshore grid connection). These additional locations were considered as potentially yielding more power. The coordinates of the locations are provided in Table 5.1. The twenty-WEC farm is identical to the base case, with the orientation of the wave farm varied at each location to match the depth contour. In order to account for the transmission cable shore-crossing locations, we fixed 5 sub-stations in front of the locations L1 to L5 at 20 m water depth. The coordinates of the sub-stations (numbered with reference to locations) are shown in Table 5.2. The sub-station is then connected to the single onshore grid connection as defined in the base case. The wave farm layouts, sub-stations and grid connections are shown in 5.2.

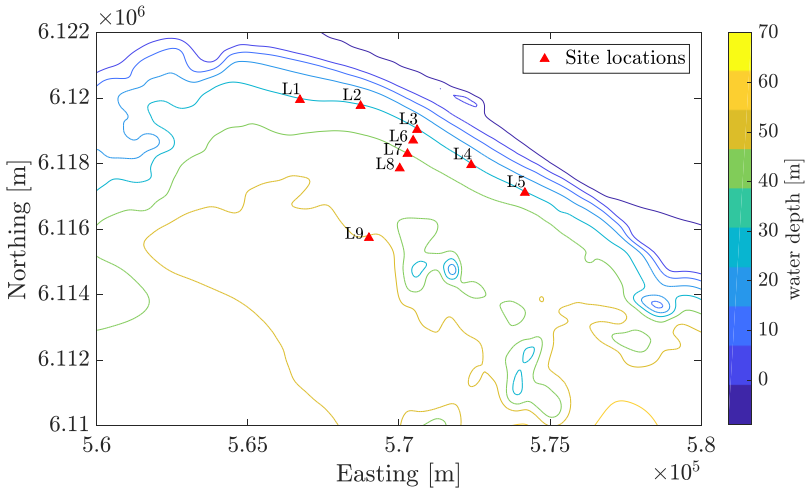

Figure 5.1. Torbay, Albany site in Western Australia. Markers indicate the considered locations for optimisation.

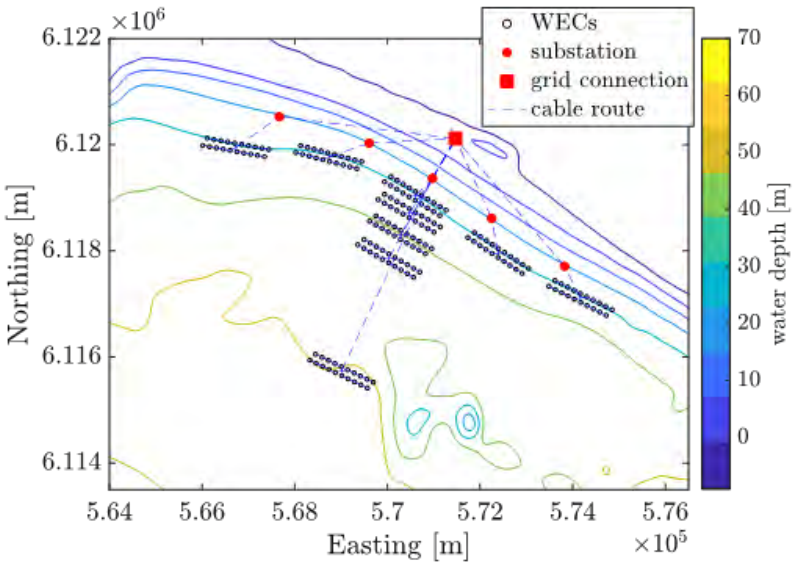

Figure 5.2. Wave farms at different locations, with the location of substations and grid connection point.

Table 5.1. Coordinates of the locations considered for phase I study (UTM zone 50 S).

Location	Easting (m)	Northing (m)	Location	Easting (m)	Northing (m)
L1	566725.45 E	6119949.54 S	L6	570470.98 E	6118709.91 S
L2	568731.98 E	6119766.97 S	L7	570284.27 E	6118302.78 S
L3	570601.13 E	6119034.38 S	L8	570027.86 E	6117859.38 S
L4	572391.03 E	6117960.18 S	L9	569008.87 E	6115734.48 S
L5	574167.17 E	6117113.45 S			

Table 5.2. Coordinates of the substations considered for phase I study (UTM zone 50 S).

substation	Easting (m)	Northing (m)
1	567665.55 E	6120527.15 S
2	569606.29 E	6120031.33 S
3	570969.91 E	6119368.06 S
4	572247.12 E	6118615.55 S
5	573825.50 E	6117709.75 S

5.1.1. Power absorption comparison

The power absorption of the wave farms at different locations are compared in a box plot in Figure 5.3.

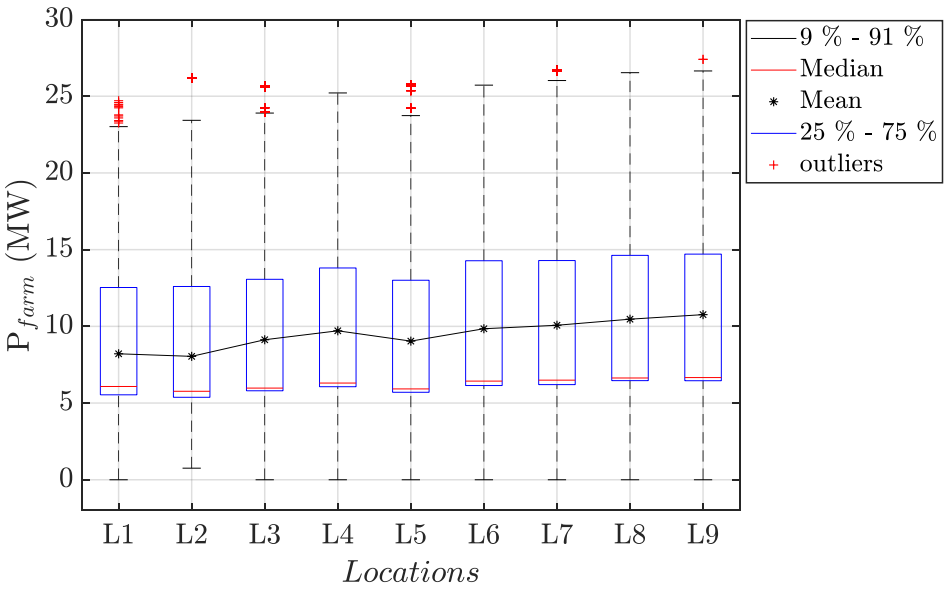

Figure 5.3. Box plot comparison for different site locations using the 38-year simulated wave data from Cuttler et al. (2020).

The maximum PTO load was fixed at 5 MN based on CCE's recommendation. For the purpose of this study, it is assumed that for sea states that exceed 5 MN PTO loading, power is not generated (i.e. the WECs are not operational, noting that in reality power is till generated, albeit at a lower efficiency). In comparing the locations that are along the 30 m water depth (L1-L5), the mean power for L4 is found to be maximum with 9.71MW (Figure 5.3). Whereas, for the locations that are placed at varying water depth (L3, L6-L9), the mean power for L9 was found to be a maximum of 10.76 MW. The mean power generated by the wave farms increased with increasing water depth.

5.1.2. Foundation engineering

Load distribution

As mentioned in Section 4.4.1, the piles were designed based on $G_S(s)$ (duration time = 3 hours). We used linear wave/structure interaction theory (Faltinsen, 1990) to calculate the $G_S(s)$ based on a 38-year wave database corresponding to the locations L1-L9. The $G_S(s)$ for locations L1-L9 are shown in Figure 5.4. It is noteworthy that the 95% quantile of load distribution used to estimate the design load never exceeds the 5 MN limit fixed on the PTO.

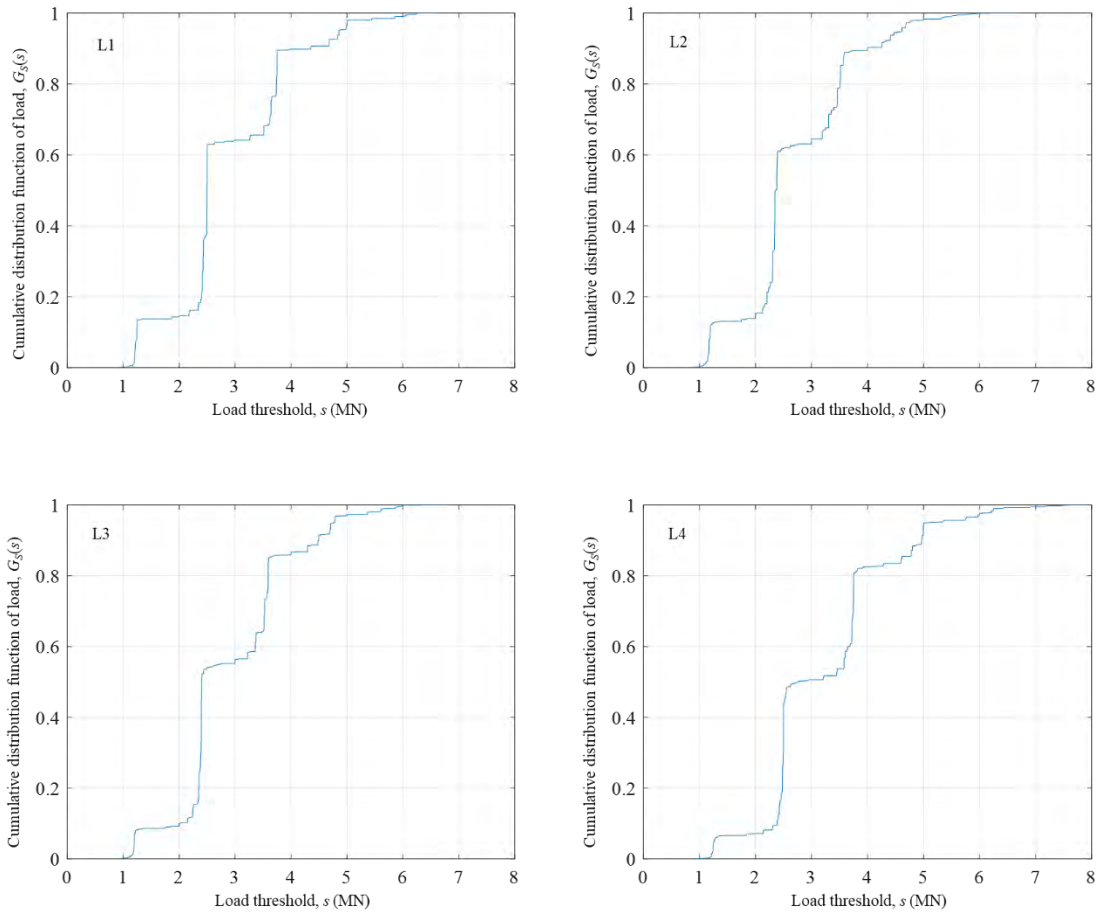

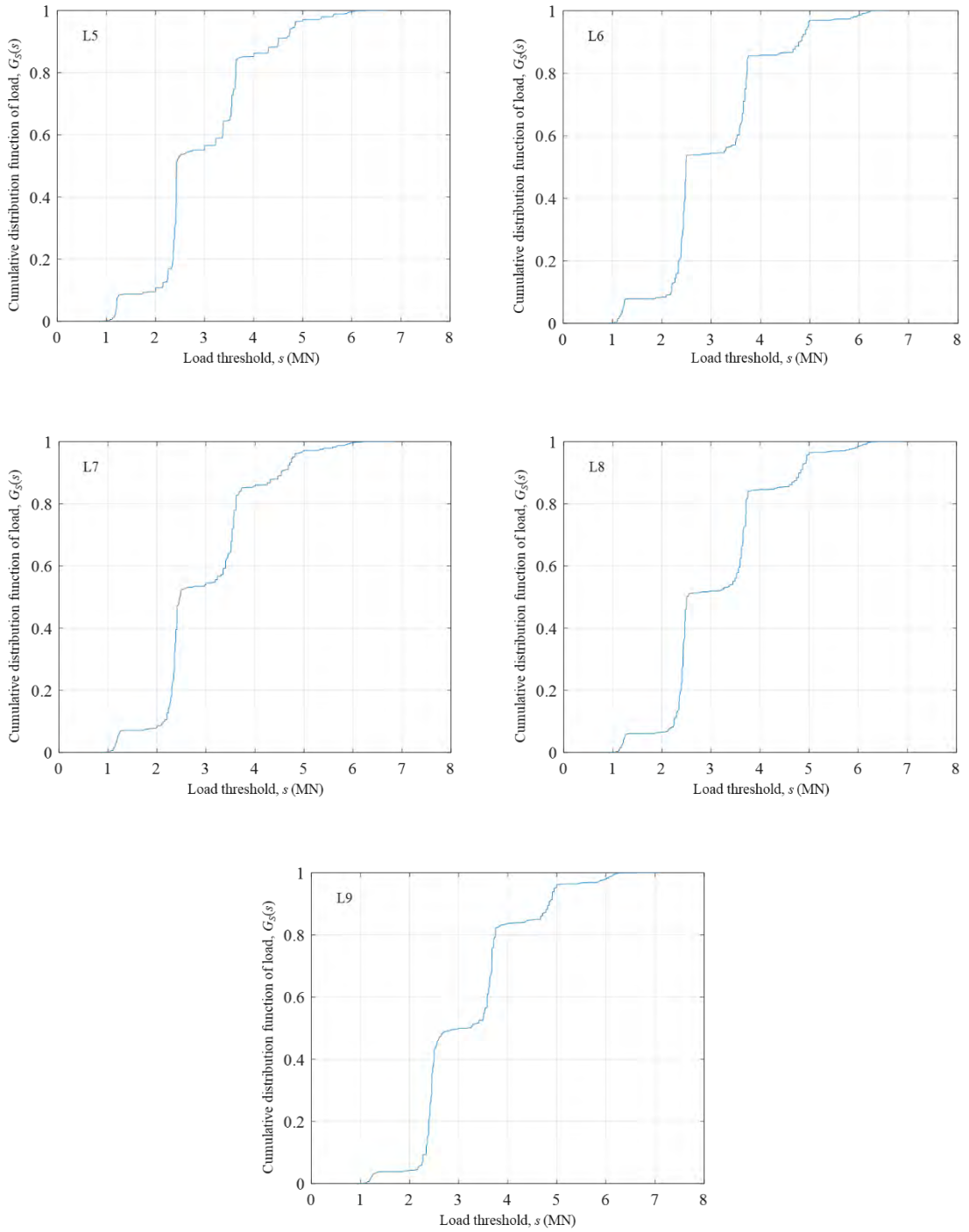

Figure 5.4. Load cumulative distribution functions for locations L1-L9

Seabed mapping

The cone tip resistance (q_c) profiles at the centre of locations L1-L9 were simulated using the random field theory presented in Section 4.4.1. Based on Eq. 13 and the water depth h of the locations L1-L9 shown in Figure 4.0.1, we calculated the mean relative density D_r values for these nine locations (see Figure 5.5). Subsequently, we calculated the depth-wise trend of q_c profiles (μ_{qc}) for the nine locations using Eq. 10. Similar to the base case, the q_c values for these nine locations were simulated as nine lognormal random fields using ($\theta_h = 40\ m,\ \theta_v = 0.9$ m, $\mathrm{COV}(q_c) =$

0.3). The q_c profiles at the measured locations (i.e. the centre points of locations L1-L9) were extracted from the random fields (see Figure 5.6).

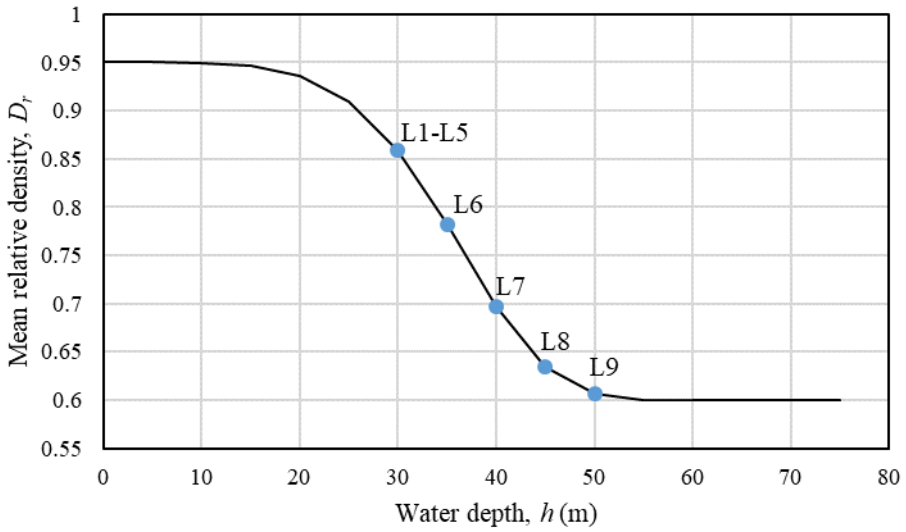

Figure 5.5. Mean relative density for soils at different water depth.

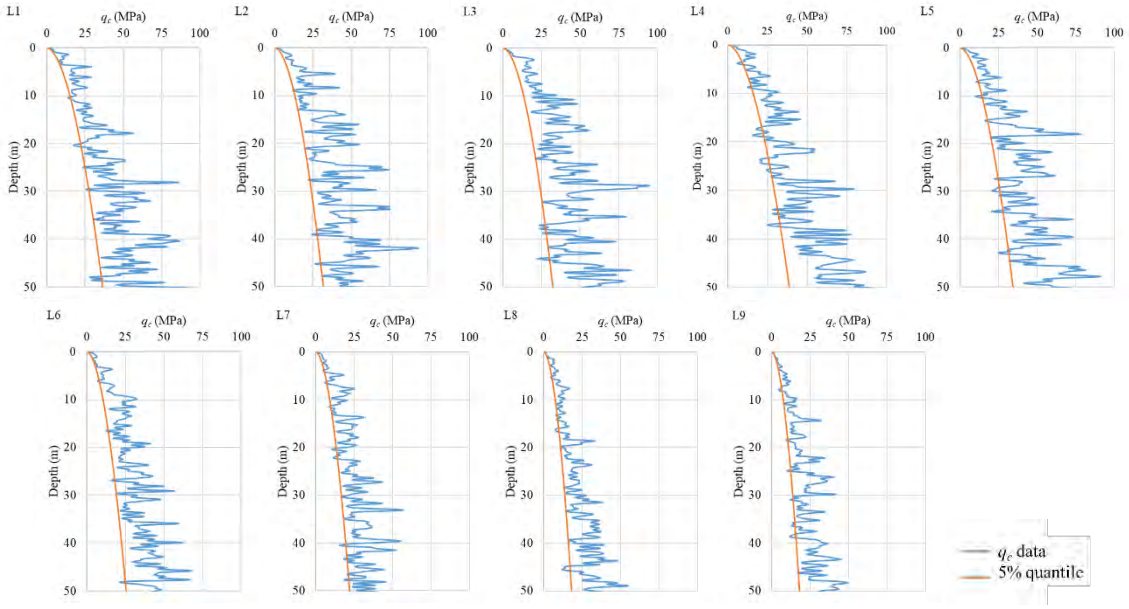

Figure 5.6. Virtual CPT data and 5% quantiles of q_c for locations L1-L9.

Pile sizing

We applied the same pile design procedure presented in Section 4.4.2 to design the piles at the locations L1-L9, which includes (1) determining the number and locations of piles; (2) calculating the design load; (3) selecting the design line; and (4) calculating the required pile length resisting the load.

Similar to the base case, the WEC array (Figure 4.2) in each wave farm is anchored by a four-row pile layout that included sixty piles.

The unfactored design loads S_{design} for locations L1-L9 were determined from the 95% quantile of the load distribution shown in Figure 5.6. Similar to the base case, the S_{design} was factored by a load factor $\gamma_L = 1.35$ and an inclined load factor $\gamma_{inc} = 0.8$, i.e. the factored design load $= \gamma_L S_{design}/\gamma_{inc}$. The calculated factored design loads $\gamma_L S_{design}/\gamma_{inc}$ for the nine locations are shown in Figure 5.7.

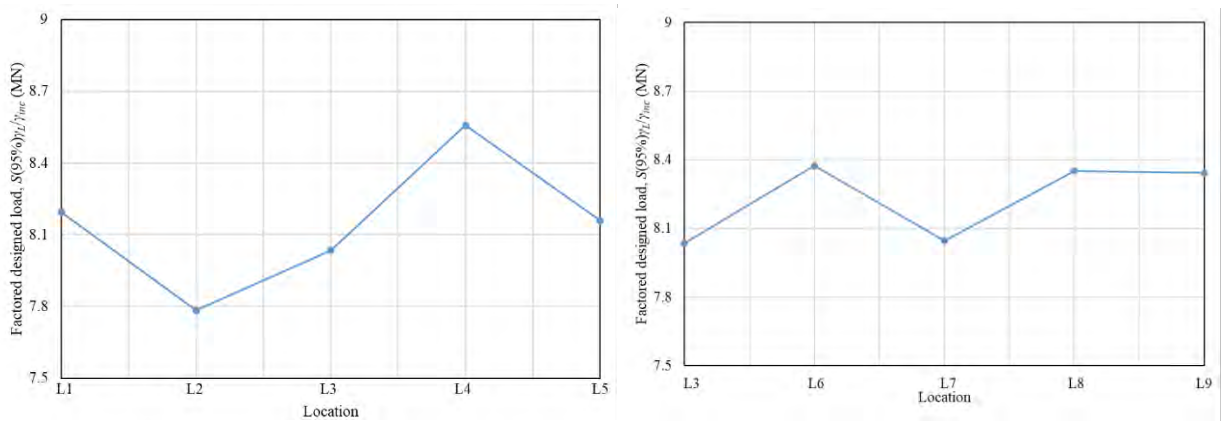

(a) (b)

Figure 5.7. Factored design load for piles at locations (a) L1-L5 (alongshore transect); and (b) L3, L6-L9 (offshore transect).

Based on the q_c profiles shown in Figure 5.6, the q_c(5%) for the locations L1-L9 can be determined using the quantile regression method (Uzielli et al., 2019). The estimated q_c(5%) profiles are also presented in Figure 5.2.3. In addition, the q_c(5%) profiles for the nine locations are summarised in Figure 5.8 for comparison. Although the mean D_r values for locations L1-L5 are identical, the difference of the q_c(5%) profiles for these five locations is significant due to the spatial random variability of the soil.

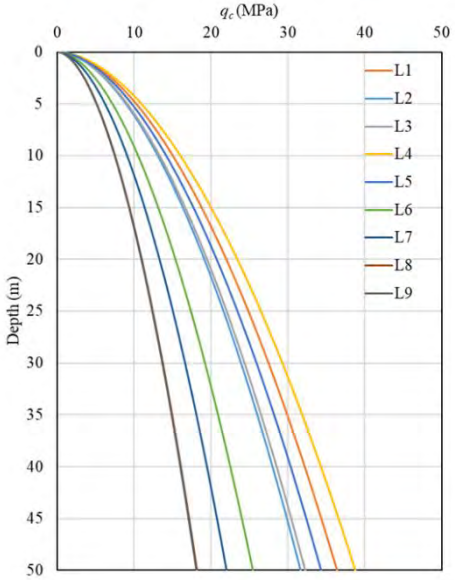

Figure 5.8. The 5% quantile of q_c profiles for locations L1-L9.

Similar to the base case, we fixed the outer pile diameter D (= 4 m) and pile wall thickness t (= 80 mm) so that only the pile length L was varied to fulfil the axial capacity requirements. The

calculated required pile length for locations L1-L9 is presented in Figure 5.9. For the candidate wave farm locations L1-L5 where the water depth is the same (= 30 m), the pile length varies due to the variability of soil characteristics and the design loads, with location L4 exhibiting the minimum pile length. As shown in Figure 5.9 the pile length increases with increasing water depth and the associated reduction in sand relative density (Figure 5.5).

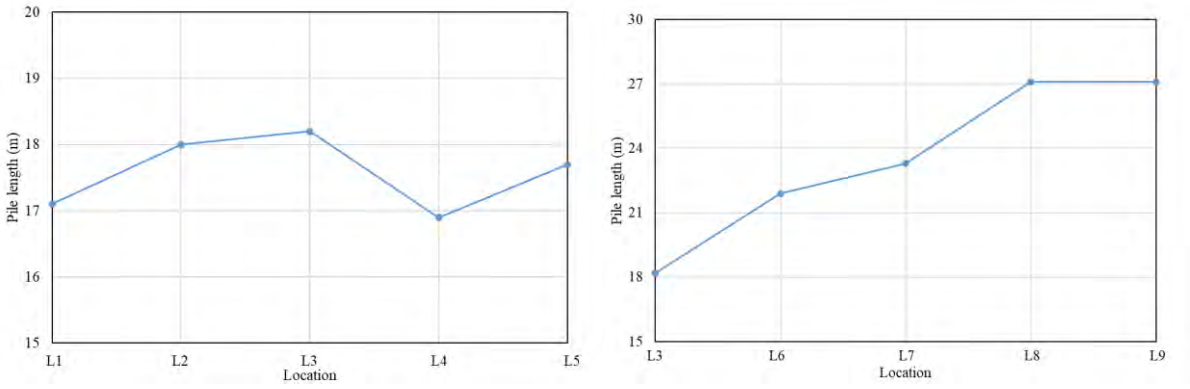

(a) (b)

Figure 5.9. Designed pile length for wave farms at site locations (a) L1-l5; and (b) L3, L6-L9.

5.1.3. Site selection

The location exhibiting the minimum ratio of total cost to mean power is identified as follows.

Foundation cost

The total foundation cost (site investigation, pile fabrication and pile installation) for the locations L1-L9 is presented in Figure 5.10.

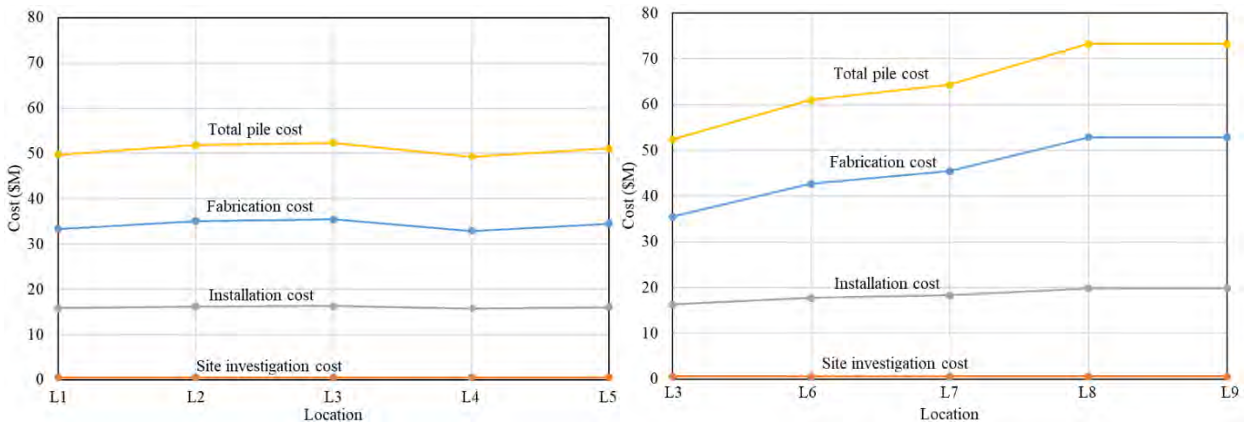

(a) (b)

Figure 5.10. Foundation cost for wave farms at locations (a) L1-l5; and (b) L3, L6-L9.

The site investigation cost is the same for the nine locations since we applied the same strategy for these locations (i.e. one CPT in the centre of the array). The installation cost varies as a function of the pile length and required installation time. The fabrication cost is directly proportional to the pile length and constitutes the largest fraction of the total cost. As highlighted in Figure 5.10, location L4 exhibits the lower foundation cost (= $49.272M). Compared to the pile cost for the

base case (= $52.323M), a $3.051M (5.8%) pile cost saving would be achieved by re-positioning the wave farm from L3 to L4.

Cable length and cable cost

The required cable length and cable cost are plotted in Figure 5.11. The cable length and cable cost are dependent of the water depth and the distance between the wave farm and the substation. As shown in Figure 5.11, location L3 has the shorter cable length (4234 m) and lower cable cost ($5.323M).

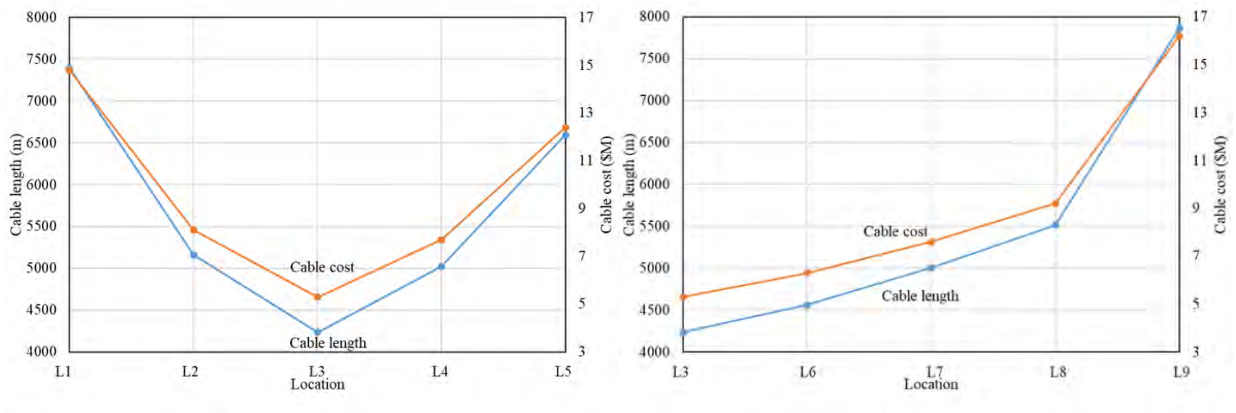

(a) (b)

Figure 5.11. Cable length and cable cost for wave farms at locations (a) L1-l5; and (b) L3, L6-L9.

Total cost

The foundation cost, cable cost and total cost for the nine locations are plotted in Figure 5.12. The minimum total cost ($56.966M) was achieved for the wave farm located in L4, for which the increase in cable cost compared to L3 is offset by a higher saving in foundation.

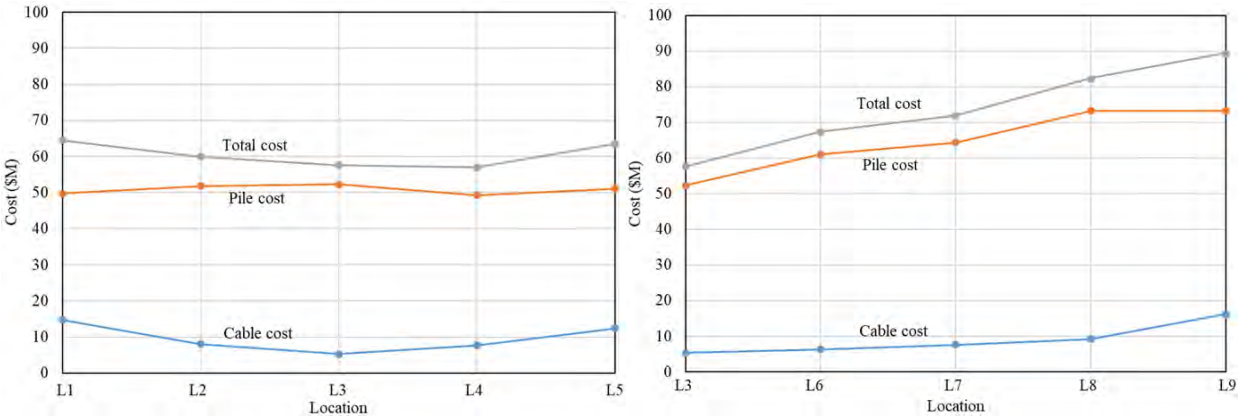

(a) (b)

Figure 5.12. Total cost for wave farms at locations for wave farms at locations (a) L1-l5; and (b) L3, L6-L9.

Normalised total cost

To determine the optimal location of the wave farm, we normalised the total cost shown in Figure 5.12 by the mean power output shown in Figure 5.3. The normalised cost for the nine locations is plotted in Figure 5.13, which indicates that location L4 exhibits the lowest normalised cost at

$5.867M/MW. This represents a saving of $0.449M (7%) compared to the normalised cost of $6.316M/MW established for the base case.

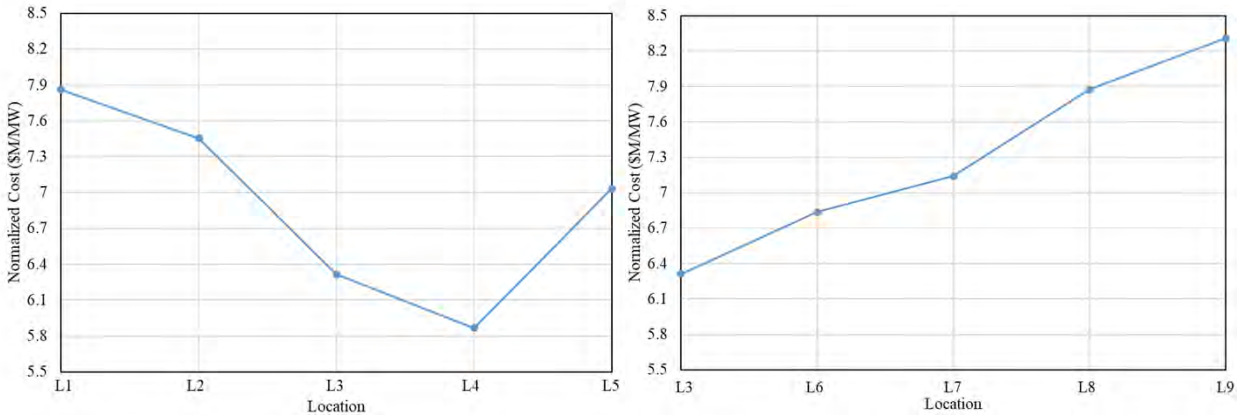

(a) (b)

Figure 5.13. Normalised total cost for wave farms at locations (a) L1-l5; and (b) L3, L6-L9.

It is useful to note here that Figure 5.13 does not include total cost of the development, and only the cabling and foundation infrastructure cost. Including the total cot may result in a different optimal location in this specific case, whitout however modifying the approach and outcomes presented in phase II.

5.2. Phase II: Site optimisation

The optimal location of the wave farm being identified, the next step consists in optimising the array configuration using a multi-objective optimisation technique.

5.2.1. Multi-objective optimisation of wave farms

Unlike the single-objective optimisation, multi-objective optimisation deals with a set $f = \{f_1, f_2, ..., f_n\}$ of n objective functions simultaneously. Furthermore, instead of finding one optimal solution, multi-objective optimisation aims at finding a set of non-dominated (also called *Pareto* optimal) solutions subject to constraints. For more details on non-dominated solution/sorting, readers are referred to Birk (2009) and Deb et al. (2000). The concept of multi-objective optimization is not new, with several existing studies having applied the framework in different fields, e.g., WEC geometries, (Kurniawan and Moan, 2013), offshore structures (Birk, 2009) and wind farms (Karimi et al., 2017; Rodrigues et al., 2016). In this report, we apply the multi-objective optimisation approach to the CETO-6 wave farms at location L4. While the method can be applied to a myriad of parameters to optimise, we optimised the array to maximizing power generation and minimise the transmission cable length connecting each WEC in the farm to a sub-station. We utilised the evolutionary multi-objective optimisation framework (also referred to as the MOEA approach) following Deb (2011). Similar to existing studies, we used a population-based multi-objective optimization strategy and fixed the population size (*PopSize*) as sixty based on our initial trials with five and seven-WECs optimisation. The optimization procedure involves five broad steps: (i) initializing the wave farms (arrays), (ii) evaluating each objective function for each array (i.e. power production and cable length), (iii) non-dominated sorting to identify the *Pareto* optimal

solutions, (iv) generating new wave farms by variation of the non-dominated solutions and (v) repeating steps (i) to (iv) until the specified stopping time.

Several existing theoretical studies (e.g. (Babarit, 2013; Falnes, 1984) have shown that linear arrays with optimal inter-device spacings in relation to the incoming wavelength increase power absorption through constructive interference e.g., (Babarit, 2013; Falnes, 1984). Therefore, we based the optimisation around linear arrays with the array variables to be optimised including inter-device spacing of WECs (S_k), the orientation of the farm (θ_k), the number of rows (r_k) and spacing of rows (S_{rk}). We call this array model *linear array* (*LA*). The variables are subjected to the following constraints:

$$\begin{cases} 100\,m \le S_k \le 300\,m \\ 0° \le \theta_k < 360° \\ 50\,m \le S_{rk} \le 300\,m \\ r_k = 1,2,3\,rows \end{cases} \qquad \forall k = 1, 2, \ldots, PopSize. \qquad \text{Eq. 21}$$

The orientation of the mooring arrangement is fixed in relation with the orientation of the wave farm. For example, when θ_k = 0°, the mooring arrangement is fixed with one tether pointing in offshore in the direction of wave approach and the other two obliquely oriented in the onshore direction. Once the array is initialised based on the aforementioned method, the optimisation procedure described in Figure 5.14 is applied.

Objective functions

Maximising power generation is the first objective considered in the optimisation. We used the interaction factor, also called the 'q' factor (Babarit, 2013), which is the ratio of the power absorbed by the array to N times that produced by an isolated WEC (P_{iso}):

$$q = \frac{P_{mean}}{NP_{iso}} \qquad \text{Eq. 22}$$

As we focused on minimizing the objective functions, we used $1/q$, instead of q, as the first objective function.

Minimizing the shortest cable distance (L_c) connecting all WECs in the farm to a sub-station (for minimizing the length of transmission cables) is the second objective function. For this, we utilised *Prim's* algorithm (Prim, 1957). Given the undirected weighted graph (V, E, w), where V, E, w are the vertices, edges and weights (distance) connecting the source s and target t WECs, the length of cable is

$$L_c = \sum_{st \in E} w_{st} \qquad \text{Eq. 23}$$

We normalised L_c by N *(=20 WECs)* times the minimum spacing, S *(=100 m)*, and used it as the second objective function.

Once the objective functions are evaluated for the wave farms generated in the first iteration, the solutions are subjected to a non-dominated sorting to identify the *Pareto* fronts which will be used to generate the new offsprings (arrays). The evolutionary strategy to generate new offsprings is one crucial part of the optimisation as it influences the convergence rate of the optimal solutions. A recent study (Neshat et al., 2020) presents a comprehensive comparison of different evolutionary strategies and convergence rates of the optimal solution for a single-objective optimisation. In this study, we used a probability based evolutionary strategy. The new Cartesian

coordinates in the offspring are generated based on a combination of normal and uniform distributions. The inter-device spacing S_k and row spacing S_{rk} are obtained from a normal distribution with mean 0 and standard deviation σ which changes with each iteration as:

$$\sigma = \frac{1}{G^c} r_{max} \qquad \textit{Eq. 24}$$

where G is the iteration number, r_{max} is a pre-selected radius of 250 m and c is a mutation coefficient chosen as 0.2 based on our initial trials with a 5-WECs array optimisation. Further, θ_k is obtained from a continuous uniform distribution, whereas r_k is obtained from discrete uniform distribution subject to the constraint. The new arrays are then evaluated, and the optimisation procedure described in Figure 5.14 is repeated until the assigned stop time.

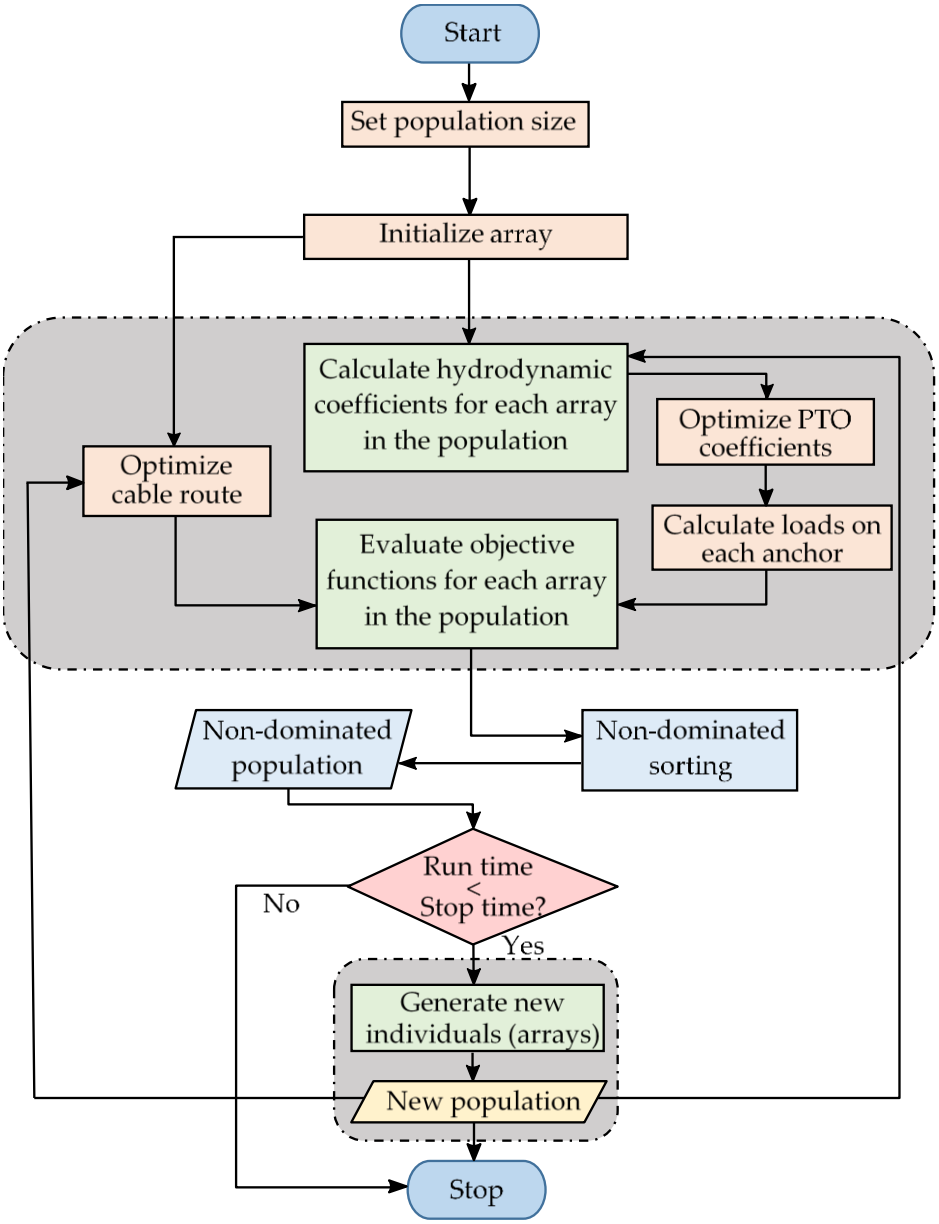

Figure 5.14. Flow chart of the multi-objective optimization.

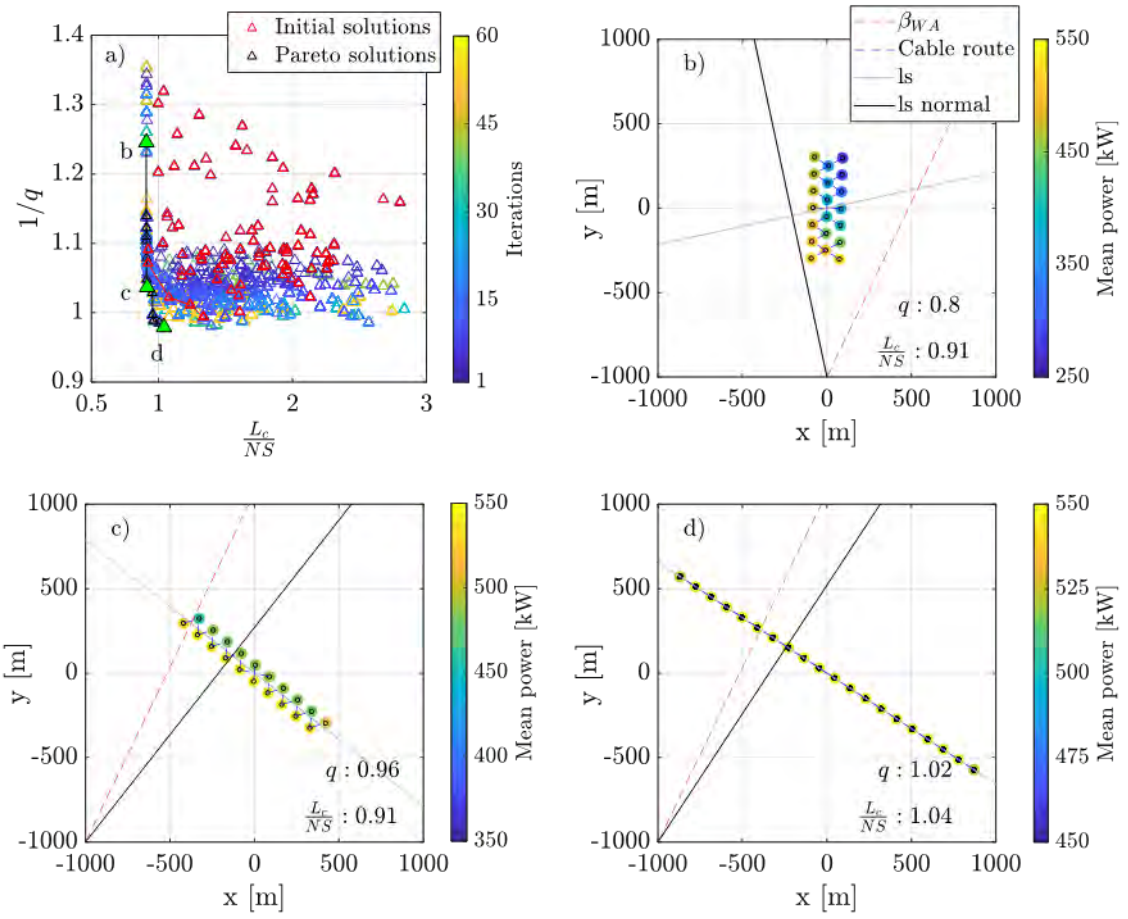

Figure 5.15. Multi-objective optimisation for 20-WECs. In panel a), the axis represents 2 objective functions i.e., x – normalised cable length, y – inverted q factor. The green highlighted layouts in panel a) are shown in panels b, c, d respectively. The black circle in panels b, c, d shows the device diameter (= 25 m).

Figure 5.15 shows the multi-objective optimisation for twenty WECs using the wave conditions from location L4. The convergence of the *Pareto* front from the initial solutions can be distinguished with the colourbar) in Figure 5.15a. As it is not feasible to show all the candidates in the *Pareto* front, some selected layouts are highlighted in panel Figure 5.15b, c, d, respectively. The wave farm layout with maximum power converged as a single row of WEC with the least square axis (*ls* axis) close to perpendicular to the weighted averaged wave angle (β_{WA}) (Figure 5.15d). The farm favouring minimum cable distance converged as multiple rows of WECs (Figure 5.15b), whereas the wave farm close to favouring both objective functions converged as two rows of WECs, (Figure 5.15c). For all the solutions in the *Pareto* front, the inter-WEC spacing converged between 100 and 110 m. The benefit of multi-objective optimisation is that it provides more than one solution from which the best trade-offs between the objective functions can be obtained and evaluated based on the project parameters.

As wave farms close to the shoreline may result in coastal impacts (erosion/accretion), we also used an empirical formulation (Rijnsdorp et al., 2020) to estimate the alongshore sediment transport gradient of the Pareto arrays as $\left|\frac{dQ_{ls}}{dy}\right|_{max}$:

$$\left|\frac{dQ_{ls}}{dy}\right|_{max} = 1.5e^{-1}H_s^2T_p^{-1}\left(\frac{A_w}{A_f}\right)^{0.5}\left(\frac{A_f}{L_w^2}\right)^{0.3}\left(\frac{L_w}{O_f}\right)^{0.6}\left(\frac{X_f}{Y_f}\right)^{0.1} \quad \text{Eq. 25}$$

where Q_{ls} is the sediment transport rate and y is the alongshore coordinate. Generally speaking, larger sediment transport gradients will lead to erosion and accretion which may be detrimental. The equation consists of four wave farm factors (non-dimensional groups) including; 1) the density of wave farm $\frac{A_w}{A_f}$, ($A_w = N\frac{1}{4}\pi D^2$, is the area occupied by WECs, N is the total number of WECs in the wave farm and $A_f = X_f Y_f$ is the total area of the farm, where, X_f and Y_f are the length of the farm in the *x*-axis and *y*-axis), 2) the normalised surface area $\frac{A_f}{L_w^2}$, L_w is assumed as deep-water wavelength calculated as $L_w = \frac{g}{2\pi}T_p^2$ (g is the acceleration due to gravity), 3) the normalised offshore distance $\frac{L_w}{OD}$, and 4) the aspect ratio of the wave farm, $\frac{X_f}{Y_f}$. We choose not to include the empirical sediment transport gradients as an objective function due to both the computational load and that existing studies (e.g. Rijnsdorp et al., 2020) have shown generally negligible or positive coastal impacts from WEC arrays similar to those considered here. The alongshore sediment transport gradient is estimated for a range of wave climates and averaged (based on the number of occurrences of each sea state) to compare for different wave farms in the *Pareto* solutions. The objective function values along with the mean alongshore gradient estimate for all the *Pareto* solutions is shown in Figure 5.16.

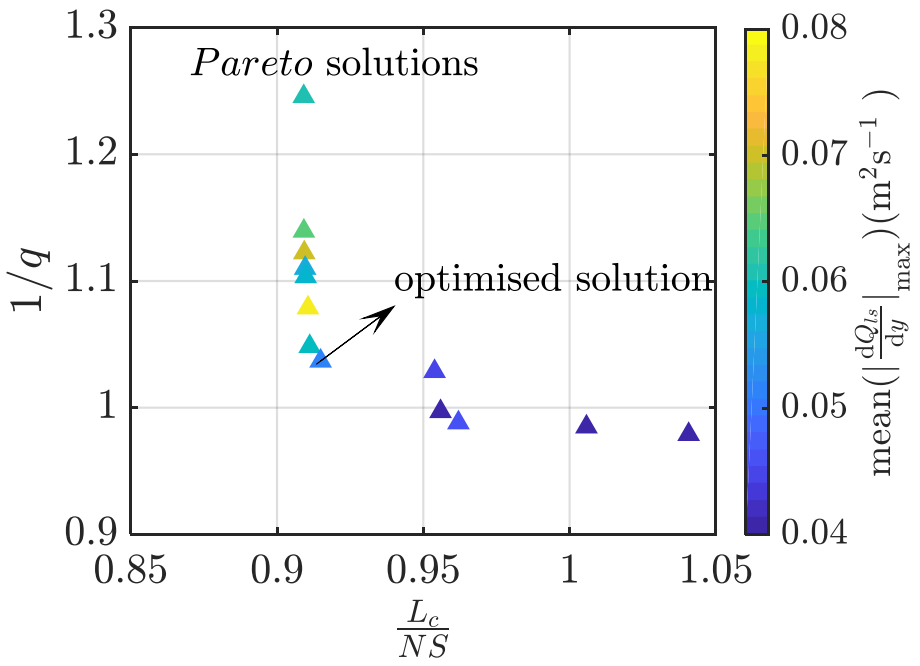

Figure 5.16. Pareto solutions from 20-WEC optimisation. The axis represents 2 objective functions i.e., x – normalised cable length, y – inverted q factor and the color implies the mean alongshore sediment transport gradient.

By comparing the Pareto solutions (Figure 5.16), we found the wave farm layout shown in Figure 5.17 to be optimal, in terms of minimising the objective functions as well as the coastal impacts, and it was chosen for the next stages of analysis. The wave farm variables i.e., inter-WEC spacing, row spacing, and orientation of the wave farm were optimised as 107.8 m, 55 m and 320° (anti-clockwise with respect to zero in the east and centroid of the wave farm is the pivot point). Note,

for phase I, we fixed the inter-WEC spacing and row spacing as 150 m and orientation for the L4 wave farm was fixed as 157° (Figure. 5.1, 5.2). As a result of the multi-objective optimisation and subsequent PTO optimisation for each WEC in the array, the mean power output for this layout (Figure 5.17) increased from 9.7MW (L4 farm from Phase I) to 10.2 MW. The cable length components for the optimised layout is shown in Table 5.3

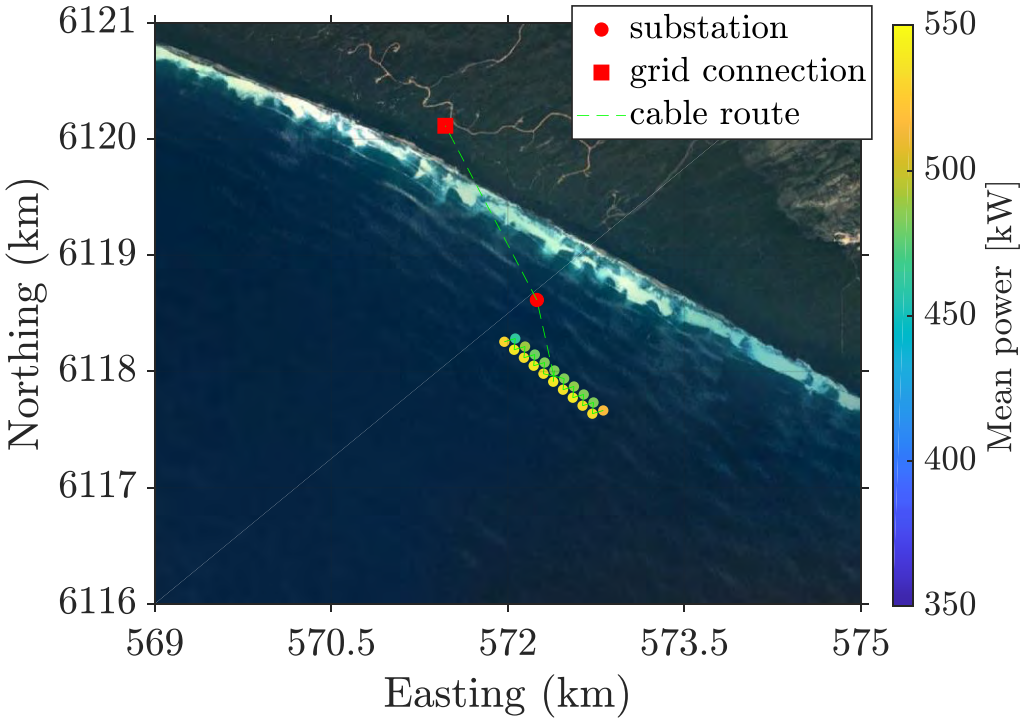

Figure 5.17. Optimised twenty-WEC farm at L4 location.

Table 5.3. Length of cable for the optimised wave farm in L4

Site Locations	Within array (m)	Wave farm to substation (m)	Substation to the grid connection point (m)	Total (m)
L4	1830	497	1689	4016

5.2.2. Optimisation of foundation design

The last step of the optimisation process consists in (i) identifying the optimal level of site characterisation leading to a less conservative and more economical foundation design and (ii) optimising the foundation design by better understanding the foundation performance under the specific loading conditions generated by the CETO 6 device. The cost model described in section 4.5.2 is used again.

Calibration of characteristic design line

In the base case, the piles were designed using the 5% quantile of q_c from a single CPT. The 5% sample quantile is a conservative assumption usually assumed in practice when the soil

characteristics are unknow or exhibit a variability which is not sufficiently characterised. Best practice might consider performing a borehole and CPT at the location of each of the sixty foundations, but this approach could be cost prohibitive in the sense that the savings generated on the foundation may be offset by the cost of the soil characterisation. For a given site and given conditions, there is an optimal number and location of CPTs that would lead to a minimum total cost of site characterisation and foundation engineering. The following procedure aims to find this.

This step quantifies the probability of failure (p_f) of a pile designed using different sample quantiles (SQ = 5%-95%, in 5% increments) of CPT (q_c) data that is d meters away from the centre of the pile (e.g. Figure 5.18). The probability of failure is defined as the probability that the environmental load exceeds the pile capacity. We calculated the cumulative probability distribution function of the load, $G_S(s)$ for the optimised WEC array (shown in Figure 5.17) using the method demonstrated in Section 4.4.2 and shown in Figure 5.19. Based on this load distribution, the subset simulation (SS) method (Au and Beck, 2001) was used to calculate the p_f values for different sampling quartile (SQ) values in different site conditions (i.e. different combinations of D_r, COV(q_c), θ_h, θ_v, and d). Following assembly of this data set, the optimal SQ for each condition was selected which achieved a target $p_f = 10^{-4}$, typically used for design.

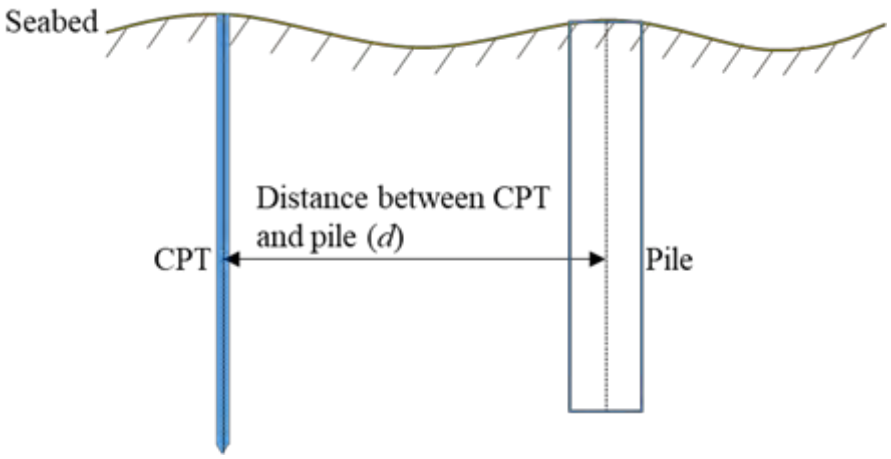

Figure 5.18. Sketch illustrating the relative locations of CPT and the pile.

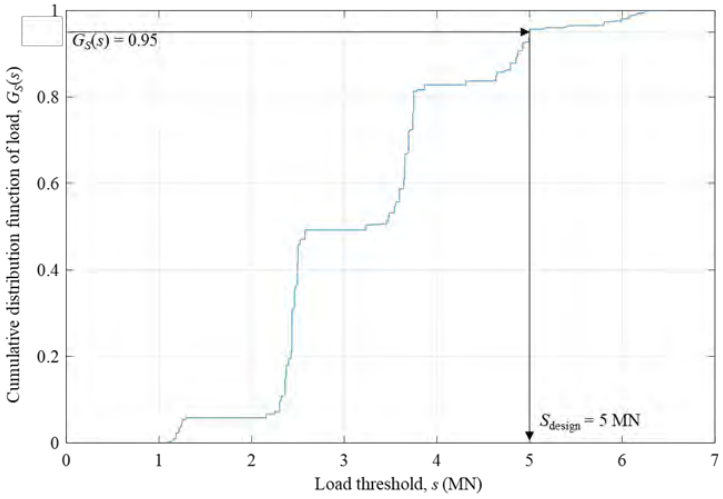

Figure 5.19. Empirical load cumulative distribution function for the optimised WEC array at location L4.

For example, Figure 5.20 plots the probability of failure for the investigated SQ values when D_r = 85%, COV(q_c) = 0.3 (lognormal distribution), θ_h = 40 m, θ_v = 1.5 m and spacing, d = 0. The p_f data points are linearly interpolated to construct a continuous SQ-p_f curve. The p_f increases from 2.09 × 10^{-6} to 3.0 × 10^{-2} with SQ increasing from 5% to 95%. This trend is expected because the design line becomes less conservative with the increase of SQ. For this site condition, the SQ value which achieves a p_f of 10^{-4} is 34.7% and so this is the value selected for use in design. By comparing to the SQ = 5% applied in previous calculations, the optimal SQ for this specific site condition uses a soil strength 44% higher than the base case.

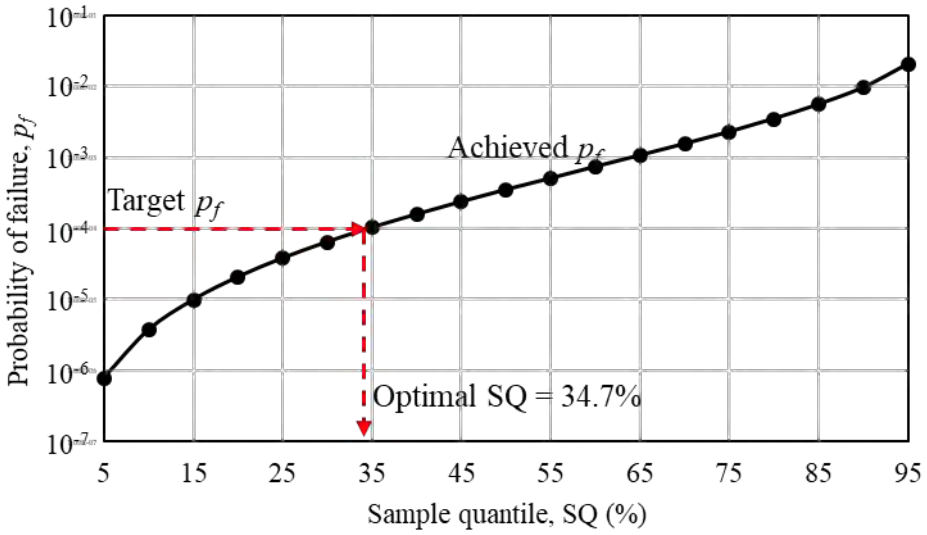

Figure 5.20. Variation of probability of failure with sample quantile.

Table 5.4. Summary of parameters explored in the characteristic design line calibration.

Parameter	Symbol	Property
Distribution of q_c	--	Lognormal distribution
Relative density (%)	D_r	65, 75, 85, 95
Coefficient of variation	COV(q_c)	0.1, 0.2, 0.3, 0.4, 0.5
Horizontal scale of fluctuation (m)	θ_h	1, 2, 3, 4, 10, 20, 40, 60, 80, 100, 500
Vertical scale of fluctuation (m)	θ_v	0.4, 0.9, 1.5, 2.0
Sample quantile (%)	SQ	5-95 (in 5 increments)
Normalised CPT offset distance	d/θ_h	0, 0.25, 0.5, 0.75, 1, 1.5, 2, 5, 10, 100

Following the above approach, we calculated the optimal SQs for the site conditions presented in Table 5.4. To generalise the outcomes, we normalised the spacing (d) between CPT and pile by the horizontal scale of fluctuation (i.e. d/θ_h). Phoon and Kulhawy (1999) conducted an extensive literature review and observed that the θ_h is on the order of 3–80 m (with a mean value from the reported literature of 47.9 m). The vertical scale of fluctuation θ_v is in the range of 0.1–2.2 m (with a mean value of 0.9 m). Uzielli et al. (2005) reported that the range of COV(q_c) is on the order of 0.1–0.5 (with a mean value of 0.3). Hence, the investigated θ_h, θ_v and COV(q_c) values shown in

Table 5.4 cover most of the frequently observed values for soil conditions that are relevant to marine renewable energy developments. The optimal SQs for the site conditions shown in Table 5.4 were linear interpolated to construct a continuous function SQ = $f(D_r, \mathrm{COV}(q_c), \theta_h, \theta_v, d)$, so that the optimal SQs for other combinations of soil conditions unlisted in Table 5.4 can be estimated using this function.

Foundation design using calibrated sample quantile

We used the pile design procedures shown in Figure 4.9 to design the piles for the optimised WEC array at location L4. The unfactored design load S_{design} (= 5 MN) was determined from the 95% quantile of the load distribution as shown in Figure 5.19. We used the identical load factor γ_L (= 1.35) and material factor γ_m (= 1.25) as for the previous calculations.

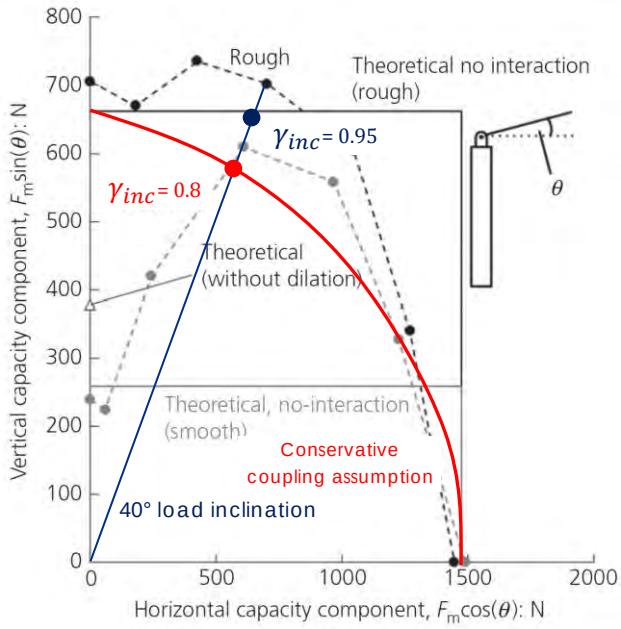

Figure 5.21. Vertical-horizontal coupling for pile under tensile inclined loading (after Huang et al. 2019.

However, the inclined load factor γ_{inc} was increased from 0.8 to 0.95 following centrifuge tests on piles in sand under loads of inclination varying from 0° to 90° from the vertical. Results, reported in Huang et al. 2019, quantified the coupling between the vertical and horizontal component of the load, and indicated that for load inclination of 40°, as relevant to the case investigated here, the coupling was beneficial and resulted in an increased capacity of the pile (see Figure 5.21). Pending further investigation exploring different sand relative densities and the detailed characterisation of the mechanisms resulting in this positive coupling, we decided here to still take a conservative, yet less punitive, approach and adopted a γ_{inc} of 0.95, leading to a factored design load $\gamma_L S_{design}/\gamma_{inc}$ = 7.11 MN. We note that adopting a γ_{inc} of 1 or 1.1 would result in further reduction of the pile length and additional cost saving.

The optimal sample quantiles quantified in Section 5.1.2 were used instead of the constant SQ = 5%. In addition, four site investigation (SI) strategies that includes one CPT, twenty CPTs, sixty CPTs and sixty-five CPTs were considered to further improve the pile design.

In order to find the optimal SQ, estimation of COV(q_c), D_r, θ_h and θ_v are necessary. The COV(q_c) is the ratio between the standard deviation (σ_{qc}) and μ_{qc}, therefore the estimation of COV(q_c) is essentially the estimation of σ_{qc} and μ_{qc}. The value of μ_{qc} can be estimated by fitting the CPT data trend using the least squared method. The σ_{qc} can be estimated by solving the following equations:

$$\begin{cases} P(\mu_{qc,ln} - \sigma_{qc,ln} < X \le \mu_{qc,ln} + \sigma_{qc,ln}) = F_{qc.ln}(\mu_{qc,ln} + \sigma_{qc,ln}) - F_{qc.ln}(\mu_{qc,ln} - \sigma_{qc,ln}) \\ F_{qc.ln}(\mu_{qc,ln} + \sigma_{qc,ln}) = 0.8415 \\ F_{qc.ln}(\mu_{qc,ln} - \sigma_{qc,ln}) = 0.1585 \\ \sigma_{qc,ln} = \sqrt{ln[1 + COV^2(q_c)]} \end{cases} \quad \text{Eq. 26}$$

where $P(\mu_{qc,\ln} - \sigma_{qc,\ln} < X \le \mu_{qc,\ln} + \sigma_{qc,\ln})$ is the probability that a random value X is located within the interval $(\mu_{qc,\ln} - \sigma_{qc,\ln}, \mu_{qc,\ln} + \sigma_{qc,\ln}]$; $F_{qc.\ln}(\cdot)$ is a normal cumulative distribution function of logarithm q_c. We assumed a cumulative distribution function because the q_c data often follows a lognormal distribution in the natural environment (Vanmarcke, 2010). In Eq. 26 the logarithm q_c values that correspond to the sample quantile of 84.15% and 15.85% can be estimated from the measured logarithm q_c data using quantile regression method (Uzielli et al., 2019). The D_r can be estimated by substituting the trend of the observed q_c data (μ_{qc}) into Eq. 10 and solving the equation. The θ_h and θ_v can be estimated by fitting the experimental correlation coefficient (estimated from the measured q_c data) with a theoretical autocorrelation function. The experimental correlation function (Baecher & Christian, 2003) used was:

$$\hat{\rho}(\tau) = \frac{1}{\hat{\sigma}_{qc}^2 k} \sum_{i=1}^{m} [q_c(a_i) - \hat{\mu}_{qc}][q_c(a_i + \tau) - \hat{\mu}_{qc}] \quad \text{Eq. 27}$$

where $\hat{\rho}(\tau)$ is the experimental correlation coefficient between two spatial points separated by τ; $q_c(a_i)$ is the q_c data at location a_i; $q_c(a_i + \tau)$ is the q_c data at location $(a_i + \tau)$ that is τ meters away from location a_i; $\hat{\sigma}_{qc}^2$ is the sample variance of q_c data; $\hat{\mu}_{qc}$ is the sample mean of q_c data; k is the total number of measured data points; and i is the total number of measured data pairs separated by distance τ. Several theoretical autocorrelation functions are available for scale of fluctuation estimation, such as single exponential autocorrelation function and squared exponential autocorrelation function (Baecher & Christian, 2003). Normally, the single exponential autocorrelation function provides the best fitting result for the scale of fluctuation estimation.

Following the above, we explored four SI strategies that includes one CPT, 20 CPTs, 60 CPTs and 65 CPTs together with the optimised SQs to design the piles and identify the most economical one.

Piles designed with a single CPT

In the one CPT SI strategy, the CPT was located at the centre of the site as shown in Figure 5.22. We then extracted the CPT data at this location from the random field defined in Section 5.1.2. Figure 5.23 shows the CPT data for the pile design case, which is the same as the CPT data for location L4 shown in Figure 4.8 as they were collected from the same location. Based on the CPT data, the statistics of q_c profile can be estimated. Figure 5.24 shows the experimental correlation coefficient results and the single exponential autocorrelation function model. When the lag distance is small, the experimental correlation coefficients are positive, and they can be well fitted by the selected autocorrelation function. The estimated value of θ_v using the single CPT is 1.68 m and the estimated value of COV(q_c) = 0.260 and D_r = 90.9%. We estimated the COV(q_c) by assuming a lognormal distribution of the q_c data.

By comparing to the input parameters (COV(q_c) = 0.3; D_r = 85%; θ_v = 1.5 m), the relative error for the estimation of COV(q_c), D_r and θ_v are 13.3%, 6.9% and 12%, respectively. This indicates that the COV(q_c), D_r and θ_v can be estimated by a single CPT with a relatively high accuracy. Note that the horizontal scale of fluctuation θ_h cannot be estimated from only a single CPT because there is no data pair available in the horizontal direction.

By substituting the estimated q_c statistics into the optimal SQ function SQ = $f(D_r, \mathrm{COV}(q_c), \theta_h, \theta_v, d)$, the variation of optimal SQ with θ_h and d was obtained (see Figure 5.25). By considering the uncertainty of the estimation of COV(q_c), D_r and θ_v, and the fact that θ_h cannot be measured using one CPT, the optimal SQ value (= 17.6%) was selected as the most conservative possible value in Figure 5.25.

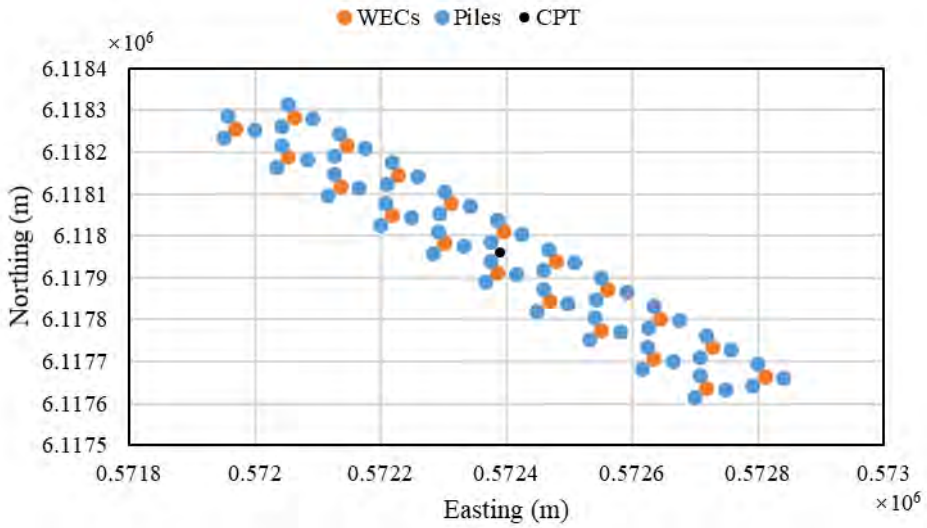

Figure 5.22. Locations of WECS, piles and CPT for the wave farm at location L4 (one CPT).

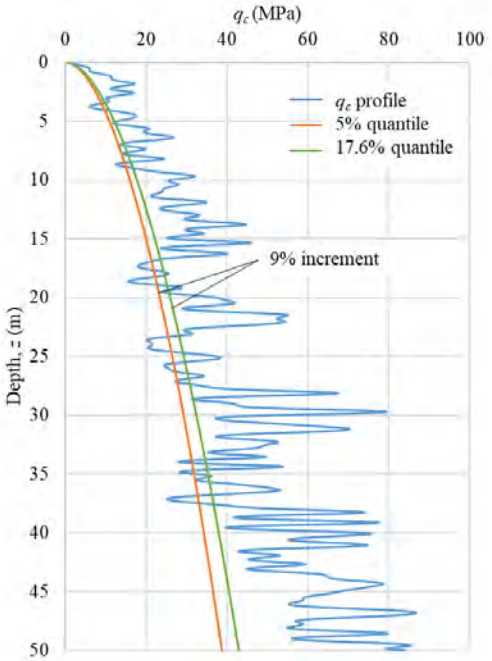

Figure 5.23. Virtual CPT data, the 5% and 17.6% quantiles of q_c for the wave farm at location L4 (one CPT).

This optimal SQ (= 17.6%) for this case using the above approach results in using a design line with 9% higher soil strength than the P5 value used in the previous design case for location L4 (in Section 5.1.2; see Figure 5.23). This results in a design pile length L = 14.6 m, which is reduced by 2.3 m compared to the Phase I outcome.

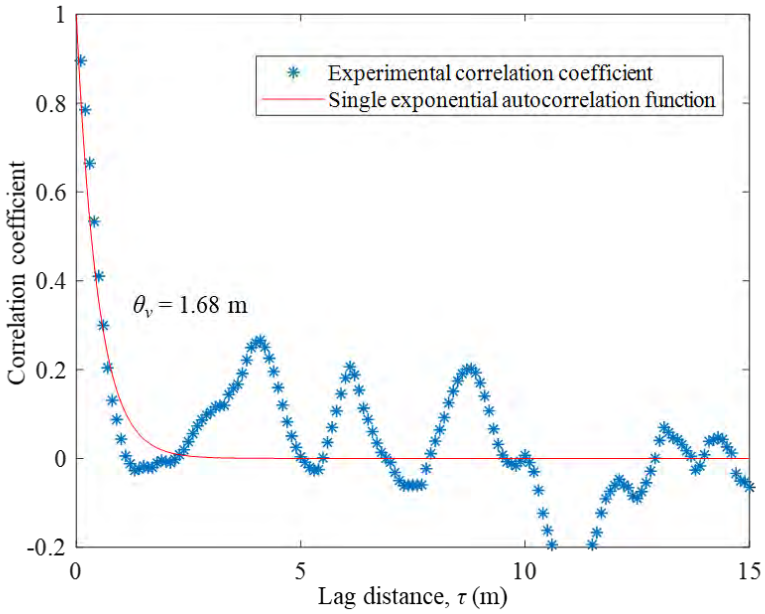

Figure 5.24. Autocorrelation structure for vertical scale of fluctuation estimation (one CPT).

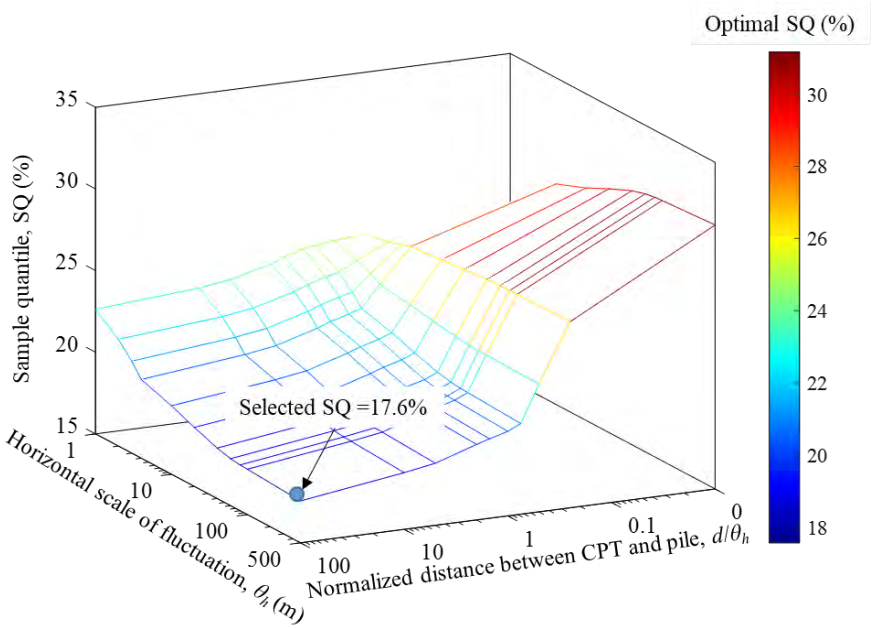

Figure 5.25. Optimal sample quantile map for different θ_h and d/θ_h (COV(q_c) = 0.260; D_r = 90.9%; θ_v = 1.68 m).

Piles designed using twenty CPTs

In this SI strategy, the twenty CPTs are located below the twenty WECs as shown in Figure 5.26, i.e. at an equal distance to the three piles anchoring each WEC. The twenty measured q_c profiles extracted from the random field are shown in Figure 5.27. Based on these CPT data, we estimated the q_c statistics of interest as: COV(q_c) = 0.299, D_r = 86.7%, θ_h = 42 m and θ_v = 1.55 m. These estimations are close to the input parameters (COV(q_c) = 0.3; D_r = 85%; θ_h = 40 m; θ_v = 1.5 m) for the generated random field.

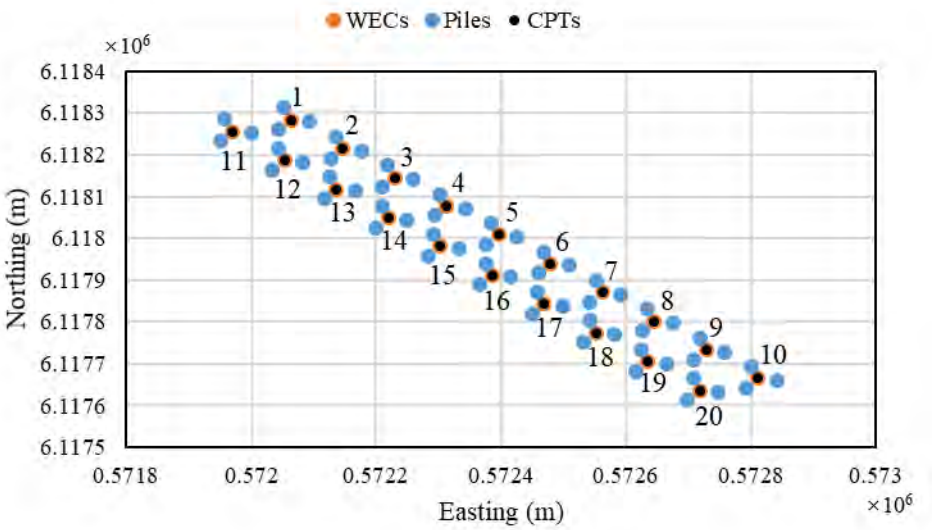

.

Figure 5.26. Locations of WECS, piles and CPTs for the wave farm at location L4 (twenty CPTs).

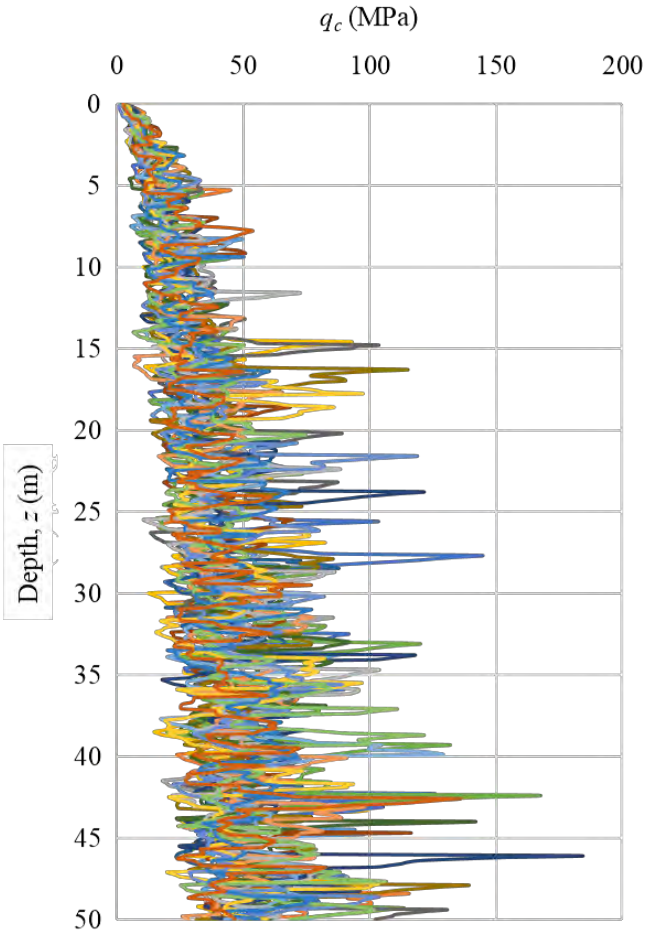

Figure 5.27. Virtual CPT data for the wave farm at location L4 (twenty CPTs).

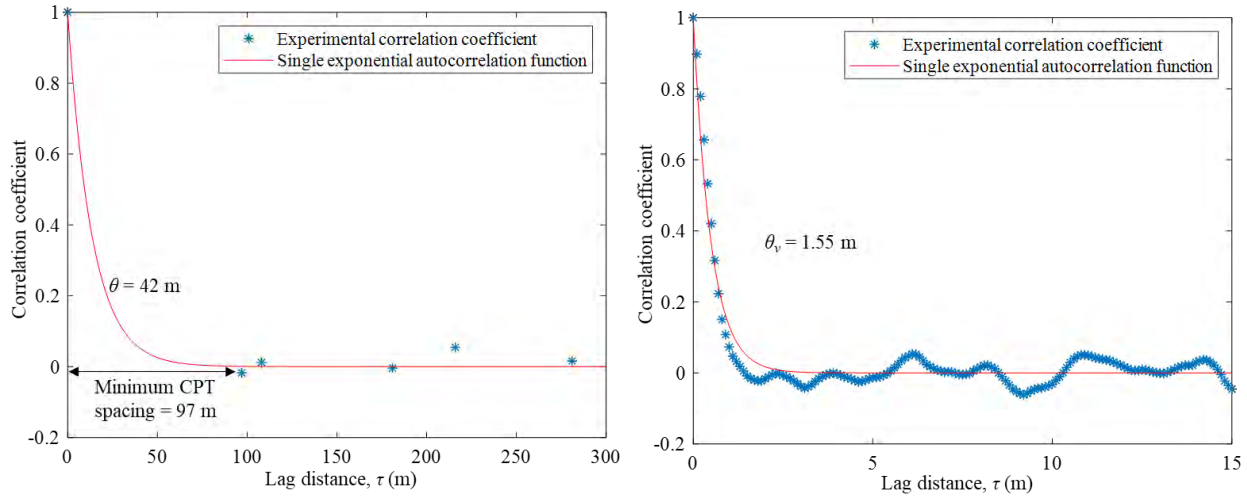

(a) (b)

Figure 5.28. Autocorrelation structure for estimation of (a) horizontal scale of fluctuation; and (b) vertical scale of fluctuation (twenty CPTs).

Following the above, the estimated COV(q_c), D_r and θ_v were substituted into the optimal SQ function SQ = f(D_r, COV(q_c), θ_h, θ_v, d), the variation of optimal SQ with θ_h and d was obtained as shown in Figure 5.28. Based on the condition that the spacing between the pile and the closest

CPT is 30 m (see Figure 5.26) and θ_h < 97 m, the trajectory of the possible optimal SQ can be identified as shown in Figure 5.29. Optimal sample quantile map for different θ_h and d/θ_h (COV(q_c) = 0.299; D_r = 86.7%; θ_v = 1.55 m). To ensure the reliability of the pile design, we selected the minimum SQ (= 24.2%) on the trajectory to design the piles. Because each pile was designed using the CPT closest to it, the q_c profiles for the piles of different WECs are different (see Figure 5.27), so that the designed pile lengths for the twenty WECs are different (see Table 5.5).

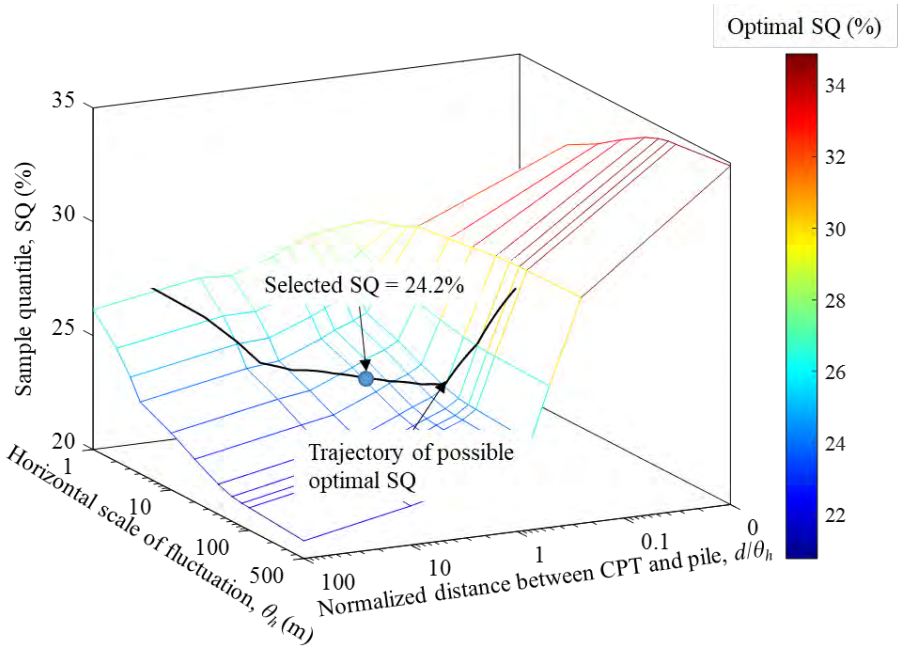

Figure 5.29. Optimal sample quantile map for different θ_h and d/θ_h (COV(q_c) = 0.299; D_r = 86.7%; θ_v = 1.55 m).

In design practice, the pile lengths for different WECs in the wave farm are usually kept the same for convenience of construction (unless the difference is significant). Therefore, in the following analysis, the mean pile length was considered as the designed pile length. In this case, the design pile length L is 13.4 m, which is reduced by 3.5 m compared to the Phase I outcome (and 1.2 m shorter than the one-CPT optimised case).

Table 5.5. Designed pile lengths for different WECs (twenty CPTs).

WEC No.	Pile length (m)	WEC No.	Pile length (m)	WEC No.	Pile length (m)
1	13.6	8	13.9	15	13.1
2	13.6	9	12.9	16	13.9
3	13.6	10	13.1	17	13.3
4	14.1	11	12.9	18	12.9
5	13.2	12	13.6	19	13.5
6	12.6	13	13.6	20	14.1
7	13.8	14	13.4		

Piles designed using sixty CPTs

In this case, each of the sixty CPTs were located at a pile location as shown in Figure 5.30. Locations of WECS, piles and CPTs for the wave farm at location L4 (sixty CPTs). The sixty measured q_c profiles extracted from the random field are shown in Figure 5.31. The statistics of interest for the sixty q_c profiles were: COV(q_c) = 0.319, D_r = 86.9%, θ_h = 39 m and θ_v = 1.43 m. Compared to the twenty CPT design case, these statistics did not change significantly. The θ_h and θ_v were estimated by fitting the experimental correlation coefficient results with a single exponential autocorrelation model (Figure 5.32). The experimental correlation coefficients in the vertical direction can be well fitted by the single autocorrelation model. In contrast, the estimated θ_h= 39 m exceeds the minimum CPT spacing (= 45 m) of the sixty CPT SI strategy. As discussed earlier, the estimated θ_h can be of any value that is smaller than the minimum CPT spacing (= 45 m), i.e. θ_h < 45 m. However, the uncertainty of the θ_h estimation is smaller compared to the twenty CPT design case because the CPTs in this configuration are closer. In addition, the distance d between the pile and the closest CPT is 0 m, which means the d/θ_h is always equal to 0 (no matter how θ_h changes). Therefore, the possible optimal SQ range for this case can be reduced to a θ_h-SQ curve by substituting the above parameters into SQ = $f(D_r, \mathrm{COV}(q_c), \theta_h, \theta_v, d)$. The estimated θ_h-SQ curve is shown in Figure 5.33. As previously, we selected the minimum SQ = 32.0% to design the pile.

The mean pile length L designed by this SQ is 13.1 m, which is reduced by 3.8 m per pile compared to the Phase I outcome.

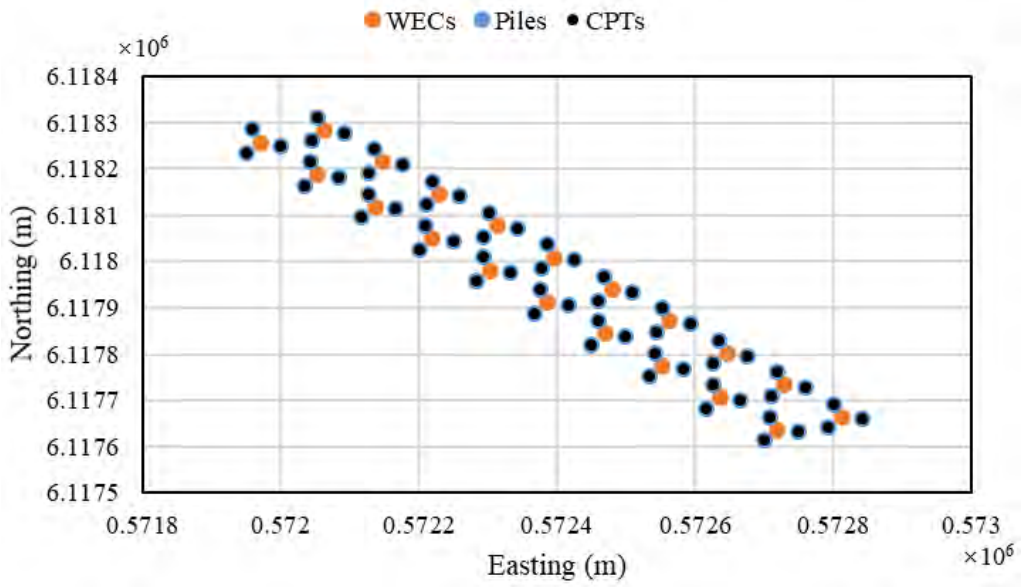

Figure 5.30. Locations of WECS, piles and CPTs for the wave farm at location L4 (sixty CPTs).

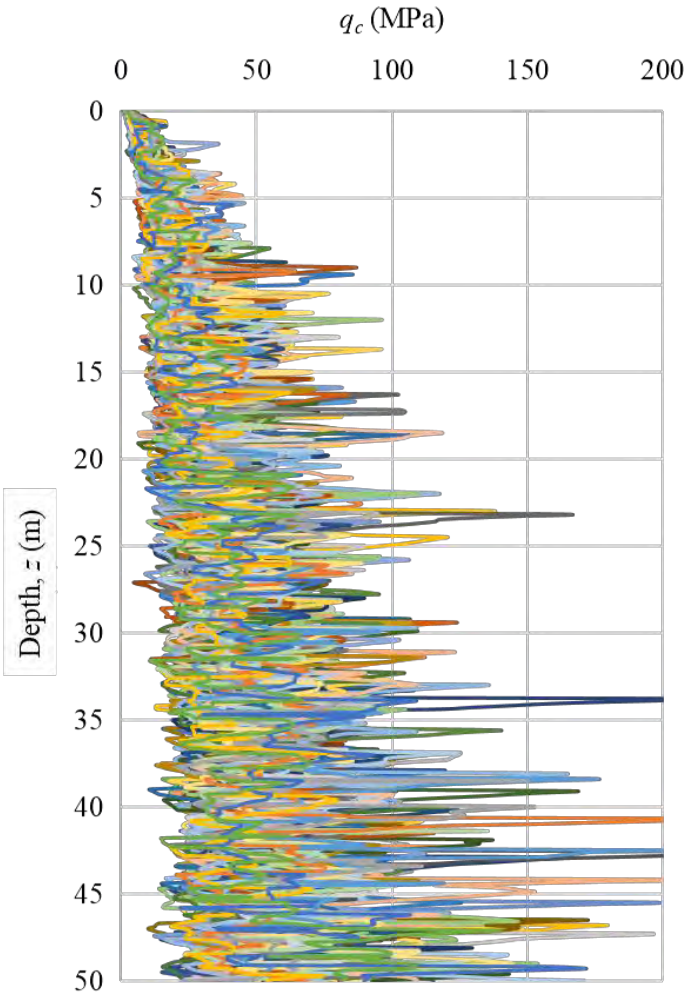

Figure 5.31. Virtual CPT data for the wave farm at location L4 (sixty CPTs).

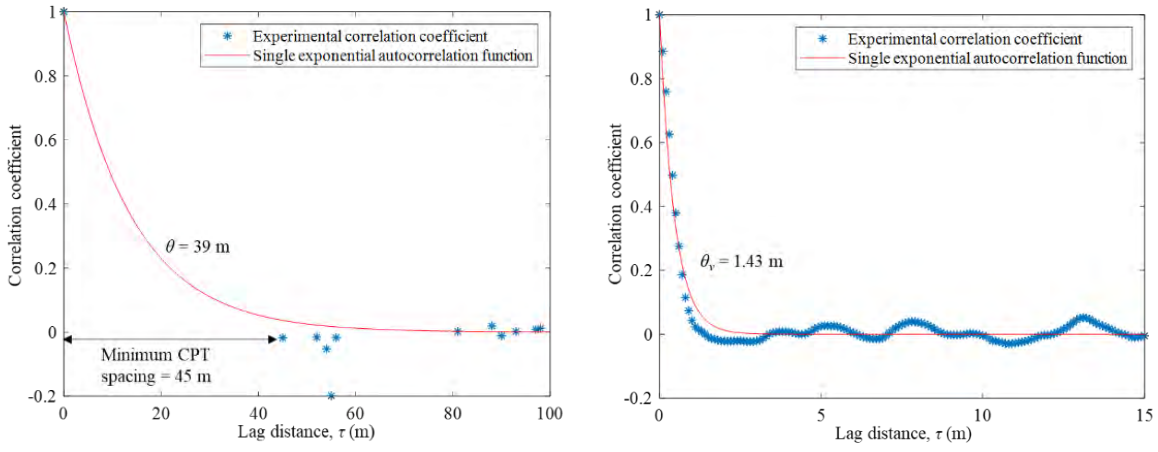

(a) (b)

Figure 5.32. Autocorrelation structure for estimation of (a) horizontal scale of fluctuation; and (b) vertical scale of fluctuation (sixty CPTs).

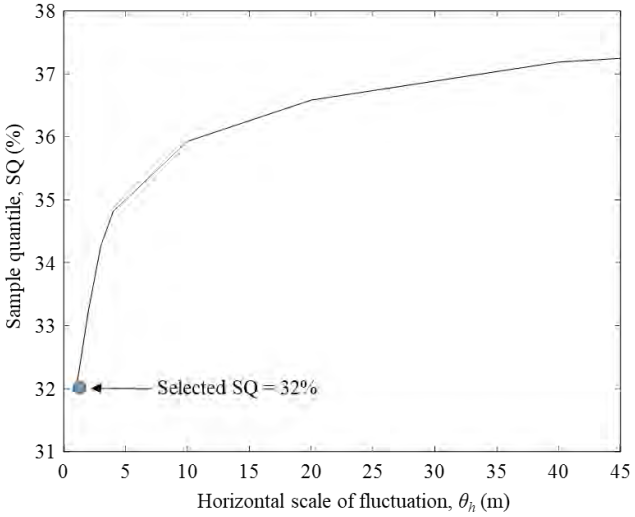

Figure 5.33. Optimal sample quantile map for different θ_h (COV(q_c) = 0.319; D_r = 86.9%; θ_v = 1.43 m; d = 0).

Piles designed by sixty-five CPTs

In the sixty CPTs case, the soil strength at every pile location was measured: This was sufficient to accurately estimate the values of COV(q_c), D_r and θ_v and reduce the maximum spacing between a pile and CPT to 0 m. However, the value of θ_h was unable to be accurately estimated because the minimum CPT spacing was larger than the estimated θ_h. Consequently, a case using sixty-five CPTs is proposed by adding five CPTs to reduce the minimum CPT spacing, therefore allowing θ_h to be estimated more accurately.

The location of the extra CPTs is shown in Figure 5.34. Figure 5.35 shows the q_c profiles. In this case, we estimated COV(q_c) = 0.318, D_r = 86.9%, and θ_v = 1.44 m. These statistics are similar to those for the sixty CPTs case because most of the q_c profiles for the statistic estimation are the same. Figure 5.36 shown the horizontal experimental correlation coefficient results and the single exponential autocorrelation function used to fit these correlation coefficient data. The estimated θ_h is 42 m. In this case, some positive experimental correlation coefficient data with a lag distance smaller than the calculated value of θ_h are available for the estimation. Therefore, the estimated θ_h becomes reliable.

By substituting COV(q_c) = 0.318, D_r = 86.9%, θ_v = 1.44 m, θ_h = 42 and d = 0 into SQ = f(D_r, COV(q_c), θ_h, θ_v, d), a deterministic SQ = 37.2% is obtained. The mean pile length designed using this SQ is 12.7 m, which is reduced by 4.2 m per pile compared to the Phase I outcome, highlighting the benefit of the additional five CPTs to estimate θ_h.

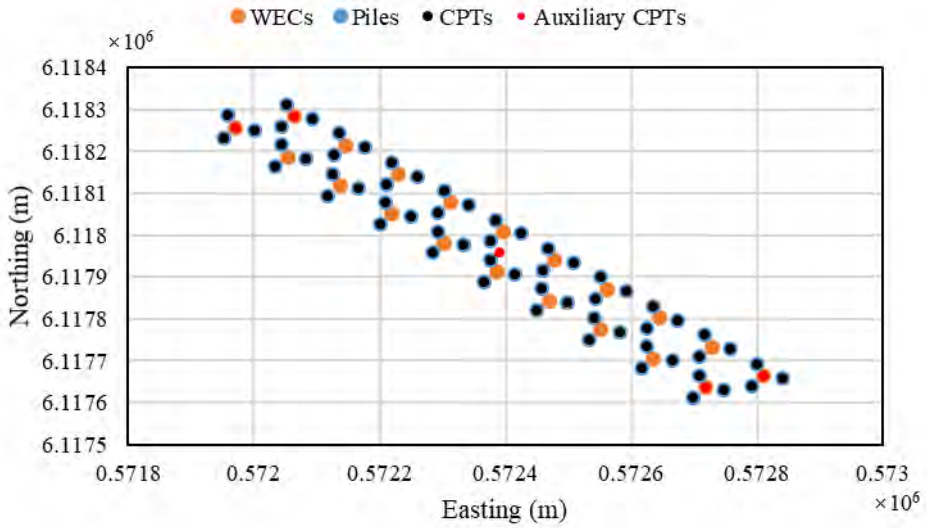

Figure 5.34. Locations of WECS, piles and CPTs for the wave farm at location L4 (sixty-five CPTs).

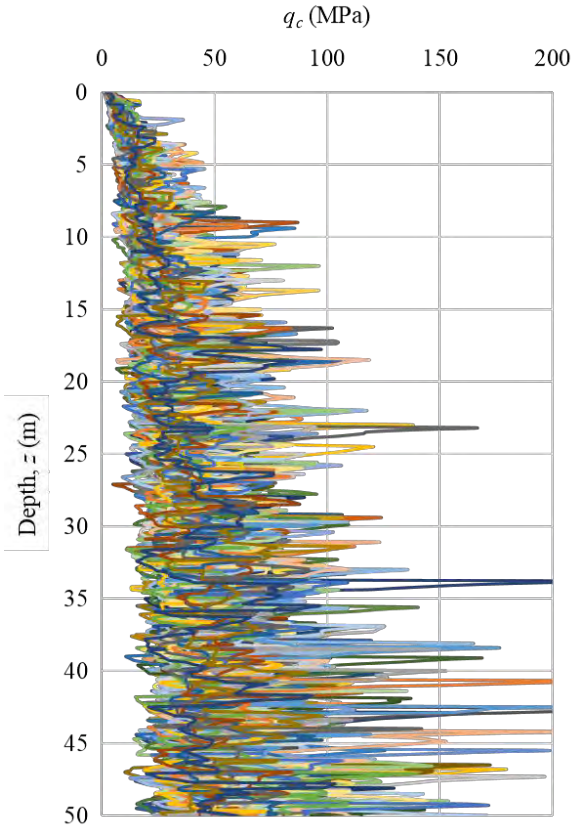

Figure 5.35. Virtual CPT data for the wave farm at location L4 (sixty-five CPTs).

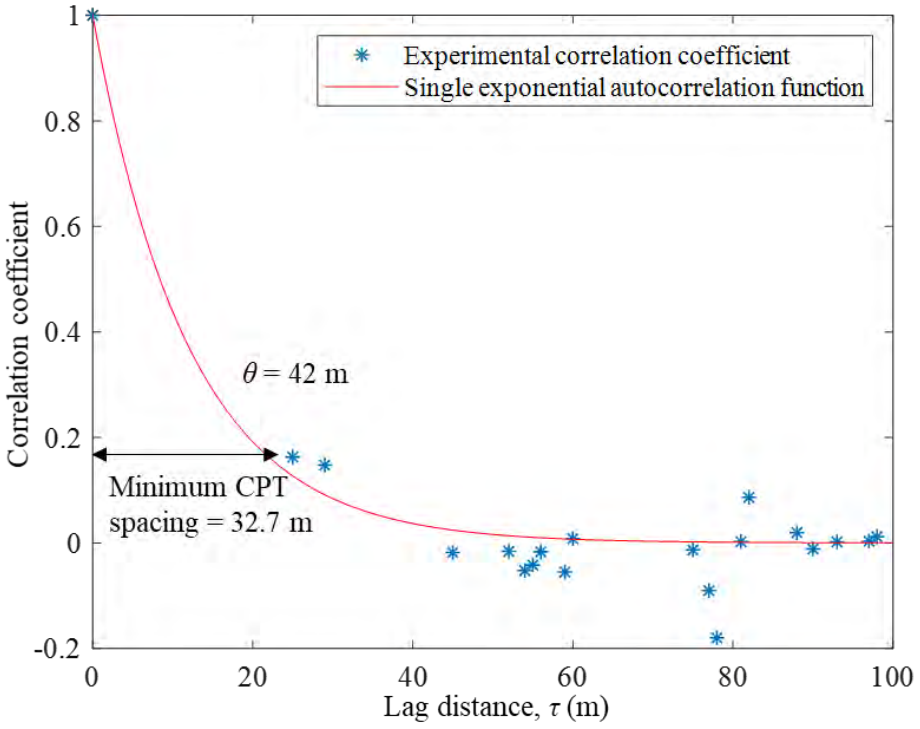

Figure 5.36. Autocorrelation structure for estimation of horizontal scale of fluctuation (sixty-five CPTs).

The designed pile length for the base case and the Phase I and Phase II cases are summarised in Table 5.6. Evidently, a higher number of CPTs results in less uncertainty in the soil conditions and a less expensive (shorter) designed pile. However, this also results in an increased site investigation cost, which needs to be balanced by the savings made on the foundation design.

Table 5.6. Designed pile lengths for different cases

Phase	Base	Opt. I	Opt. II			
Number of CPTs	1	1	1	20	60	65
Pile length (m)	18.2	16.9	14.6	13.4	13.1	12.7
Reduction to Base case (%)	--	7.1	19.8	26.4	28.0	30.2

5.3. Optimised costing

We calculated the cost of each component and the total cost using the cost model presented in Section 4.5 and compared it to the base cost presented in section 4.5.3. The results are summarised in Table 5.7. The optimal number of CPTs for the case investigated here is twenty, resulting in a reduction in foundation engineering cost of $9.8M, compared to the base case, and a $6.8M reduction compared to the phase I optimisation. When adding the reduction in cabling cost resulting from the multi-objective optimisation, the final cost reduction compared to the base case is $7.88M, lower to the reduction in foundation engineering cost due to the increase in cable cost between the base case and the optimisation phase I. However, the increase in power output needs also to be considered and this is presented in the next section.

Table 5.7. Cost of cabling and foundation infrastructure for all cases considered

Phase	Base (L3)	Opt. I (L4)	Opt. II (L4)			
Number of CPTs	1	1	1	20	60	65
SI cost ($M)	0.575	0.575	0.575	2	5	5.375
Pile fabrication cost ($M)	35.470	32.937	28.454	26.116	25.531	24.751
Pile installation cost ($M)	16.28	15.76	14.84	14.36	14.24	14.08
Total foundation cost ($M)	52.325	49.272	43.869	42.476	44.771	44.206
Cable cost ($M)	5.323	7.694	7.292	7.292	7.292	7.292
Total cost ($M)	57.648	56.966	51.161	49.768	52.063	51.498

6. Cost saving and generalisation

We calculated the normalised cost for both phases of the optimisation process and presented it compared it in Table 5.7 and represented in Figure 5.37. The final normalised cost after phase II of the optimisation process is $4.879M/MW; a reduction of 22.8% compared to the base case, and an additional reduction of 15.7% between phase I and phase II of the optimisation process.

Table 6.1. Estimated costs for different cases

Phase	Base (L3)	Opt. I (L4)	Opt. II (L4)			
Number of CPTs	1	1	1	20	60	65
Total cost ($M)	57.648	56.966	51.161	49.768	52.063	51.498
Mean power output (MW)	9.13	9.71	10.2	10.2	10.2	10.2
Normalised cost ($M/MW)	6.314	5.867	5.016	4.879	5.104	5.049
Reduction to base case (%)	-	7.1	20.6	22.8	19.2	20.1

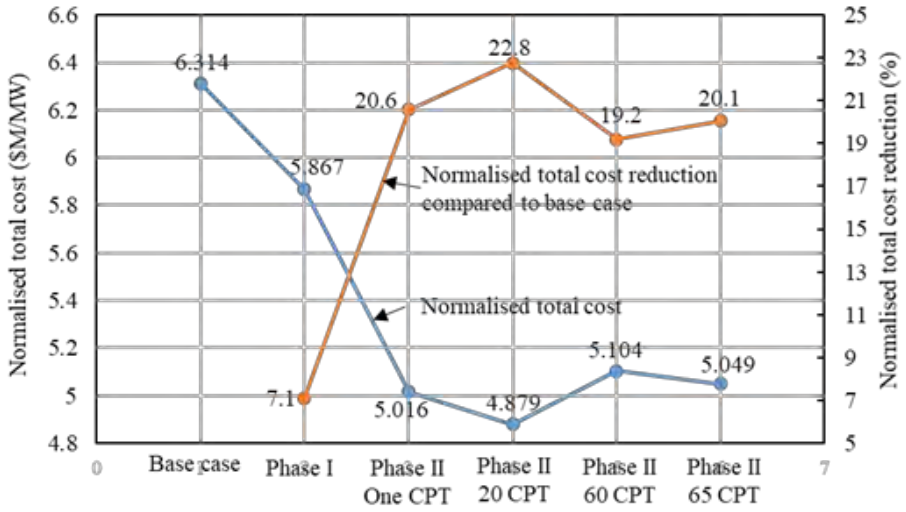

Figure 6.1. Comparison of normalised total cost among different cases.

It should be noted that the cost reduction achieved in cabling and foundation infrastructure in this project is highly dependent of the cost model assumptions made and of the variables investigated. The cost of cabling and the location of the grid connection and substation is notably an important parameter affecting the total cost. Nevertheless, the approach adopted here has demonstrated that significant savings may be generated when considering location and configuration of array of wave energy farms not only with respect to power resources, but also by considering seabed conditions and foundation engineering, for which the total cost may be significant.

The project presented in this report covers a limited number of variables. Additional savings can be generated by integrating additional key variables into the multi-objective optimisation but also by considering alternative foundation solutions that would exhibit better performance under the loading regimes generated by point absorbers.

7. References

Al Shami E, Zhang R, Wang X., 2018. Point Absorber Wave Energy Harvesters: A Review of Recent Developments. Energies.12:47.

Au, S. K., Beck, J. L., 2001. Estimation of small failure probabilities in high dimensions by subset simulation. Probabilistic Engineering Mechanics 16(4), 263–277. https://doi.org/10.1016/S0266-8920(01)00019-4.

Babarit, A., 2013. On the park effect in arrays of oscillating wave energy converters. Renew. Energy 58, 68–78. https://doi.org/10.1016/j.renene.2013.03.008

Baecher, G., Christian, J., 2003. Reliability and statistics in geotechnical engineering. Chichester, UK: Wiley.

Birk, L., 2009. Application of constrained multi-objective optimization to the design of offshore structure hulls. J. Offshore Mech. Arct. Eng. 131, 1–9. https://doi.org/10.1115/1.2957919

Bhuyan G.S., 2008. Harnessing the power of the oceans. IEA Open Energy Technology Bulletin, Issue 52.

BS-EN 1997-1:2004. Eurocode 7. Geotechnical Design. Part I; General Rules.

Budal, K., 1977. Theory for absorption of wave power by a system of interacting bodies. J. Sh. Res. 21, 248–253. https://doi.org/10.5957/jsr.1977.21.4.248.

Ching, J., Phoon, K., 2012. Value of geotechnical site investigation in reliability-based design. Advances in Structural Engineering 15(11), 1935-1945. https://doi.org/10.1260/1369-4332.15.11.1935

Cuttler, M.V.W., Hansen, J.E., Lowe, R.J., 2020. Seasonal and interannual variability of the wave climate at a wave energy hotspot off the southwestern coast of Australia. Renew. Energy 146, 2337–2350. https://doi.org/10.1016/j.renene.2019.08.058

David, D, Hansen, J, Kurniawan, A, Wolgamot, H, Lowe, R, McCauley, G., 2021. Multiobjective optimization for nearshore submerged wave farms. EWTEC 2021. (accepted)

Deb, K., 2011. Multi-objective Optimisation Using Evolutionary Algorithms: An Introduction, in: Multi-Objective Evolutionary Optimisation for Product Design and Manufacturing. https://doi.org/10.1007/978-0-85729-652-8_1

Der Kiureghian, A., Ke, J. B., 1988. The stochastic finite element method in structural reliability. Probabilistic Eng. Mech. 3(2), 83–91. https://doi.org/10.1016/0266-8920(88)90019-7

Falcão A.F.O., 2010. Wave energy utilization: A review of the technologies. Renewable and Sustainable Energy Reviews. 14:899-918.

Falnes, J., 1984. Wave-power absorption by an array of attenuators oscillating with unconstrained amplitudes. Appl. Ocean Res. 6, 16–22. https://doi.org/10.1016/0141-1187(84)90024-5

Falnes, J., 2002. Ocean Waves and Oscillating Systems: Linear Interaction Including Wave Energy Extraction, Cambridge, UK, Cambridge Univ. Press. https://doi.org/10.1007/s13398-014-0173-7.2

Falnes, J., Budal, K., 1982. Wave-power absorption by parallel rows of interacting oscillating bodies. Appl. Ocean Res. 4, 194–207. https://doi.org/10.1016/S0141-1187(82)80026-6

Faltinsen, O. (1990). Sea loads on ships and offshore structures. Cambridge University press.

Gunn K., Stock-Williams C., 2012. Quantifying the global wave power resource. Renewable Energy. 44:296-304. https://doi.org/10.1016/j.renene.2012.01.101.

Hemer M.A., Pitman T., McInnes K., Rosebrock U., 2018a. The Australian Wave Energy Atlas. Project Overview and Final Report. CSIRO. Oceans and Atmosphere, Australia. 24p.
Hemer M.A., Manassek R., McInnes K., Penesis I., Pitman T., 2018b. Perspectives on a way forward for ocean renewable energy in Australia. Renewable Energy, 127:733-745. https://doi.org/10.1016/j.renene.2018.05.036.

Huang T., O'Loughlin C.D., Gaudin C., Tian Y., Lu T., 2019. The response of rigid piles to drained tensile inclined loading. Géotechnique Letters. 9(4): 1-29. https://doi.org/10.1680/jgele.19.00028.

ISO., 2020. Petroleum and natural gas industries-fixed steel offshore structures, ISO 19902. International Standards Organization.

Karimi, M., Hall, M., Buckham, B., Crawford, C., 2017. A multi-objective design optimization approach for floating offshore wind turbine support structures. J. Ocean Eng. Mar. Energy 3, 69–87. https://doi.org/10.1007/s40722-016-0072-4

Kurniawan, A., Moan, T., 2013. Optimal geometries for wave absorbers oscillating about a fixed axis. IEEE J. Ocean. Eng. 38, 117–130. https://doi.org/10.1109/JOE.2012.2208666

Lehane, B., Schneider, J., Xu, X., 2005. The UWA-05 method for prediction of axial capacity of driven piles in sand. In Proceedings of the International Symposium on Frontiers in Offshore Geotechnics (eds M. J. Cassidy and S. Gourvenec) (pp. 683-689). The Netherlands: CRC Press, Balkema. https://doi.org/10.1061/40902(221)12

Liu, T. F., Quinteros, V. S., Jardine, R. J., Carraro, J. A., Robinson, J., 2019. A Unified database of ring shear steel-interface tests on sandy-silty soils. In: Proceedings of XVII European Conf. In: Proceedings of XVII European Conf. Soil Mech. and Geotechnical Engg. Reykjavik, Iceland.

Lunne, T., Robertson, P., Powell, J., 1997. Cone Penetration Testing in Geotechnical Practice. CRC Press.

Mantoglou, A., Wilson, J. L., 1982. The turning bands method for simulation of random fields using line generation by a spectral method. Water Resources Research 18(5), 1379-1394. https://doi.org/10.1029/WR018i005p01379

McCauley, G., Wolgamot, H., Orszaghova, J., Draper, S., 2018. Linear hydrodynamic modelling of arrays of submerged oscillating cylinders. Appl. Ocean Res. 81, 1–14. https://doi.org/10.1016/j.apor.2018.09.012

Moura Parades G., Bergdahl L., Palm J., Eskilsson C., Taveira Pinto F., 2013. Station keeping design for floating wave energy devices compared to floating offshore oil and gas platforms. Proceedings of 10th European Wave and Tidal Energy Conference, Alborg, Denmark.

Orszaghova, J., Wolgamot, H., Draper, S., Taylor, P.H., Rafiee, A., 2020. Onset and limiting amplitude of yaw instability of a submerged three-tethered buoy. Proc. R. Soc. A Math. Phys. Eng. Sci. https://doi.org/10.1098/rspa.2019.0762

Phoon, K. K., Kulhawy, F. H., 1999. Characterization of geotechnical variability. Canadian Geotechnical Journal 36(4), 612-624. https://doi.org/10.1139/t99-038

Prim, R.C., 1957. Shortest Connection Networks And Some Generalizations. Bell Syst. Tech. J. 36, 1389–1401. https://doi.org/10.1002/j.1538-7305.1957.tb01515.x

Rhinefrank K, Schacher A, Prudell J, Brekken TKA, Stillinger C, Yen JZ, 2012. Comparison of Direct-Drive Power Takeoff Systems for Ocean Wave Energy Applications. IEEE Journal of Oceanic Engineering. 37:35-44

Rijnsdorp, D.P., Hansen, J.E., Lowe, R.J., 2020. Understanding coastal impacts by nearshore wave farms using a phase-resolving wave model. Renew. Energy 150, 637–648. https://doi.org/10.1016/j.renene.2019.12.138

Rodrigues, S., Bauer, P., Bosman, P.A.N., 2016. Multi-objective optimization of wind farm layouts – Complexity, constraint handling and scalability. Renew. Sustain. Energy Rev. 65, 587–609. https://doi.org/10.1016/j.rser.2016.07.021

The Mathworks, Inc. MATLAB, Version 9.6, 2019, 2019. MATLAB 2019b - MathWorks. Www.Mathworks.Com/Products/Matlab.

Sergiienko NY, Cazzolato BS, Ding B, Hardy P, Arjomandi M., 2017. Performance comparison of the floating and fully submerged quasi-point absorber wave energy converters. Renewable Energy;108:425-37.

Statista, 2021. Electricity generation in the European Union (EU) in 2020 by fuel. https://www.statista.com/.

Ulvgård L, Sjökvist L, Göteman M, Leijon M., 2016. Line Force and Damping at Full and Partial Stator Overlap in a Linear Generator for Wave Power. Journal of Marine Science and Engineering. 4.

Uzielli, M., Vannucchi, G., Phoon, K. K., 2005. Random field characterisation of stress-normalised cone penetration testing parameters. Géotechnique 55(1), 3–20. https://doi.org/10.1680/geot.2005.55.1.3.

Uzielli, M., Zei, M., Cassidy, M. J., 2019. Probabilistic Assignment of Design Undrained Shear Strength Using Quantile Regression. In Proceedings of the 7th International Symposium on Geotechnical Safety and Risk (ISGSR 2019).

Vanmarcke, E., 2010. Random Fields: Analysis and Synthesis. Revised and Expanded New Edition. Beijing: World Scientific Publishing.

Oceans Graduate School |
T +61 8 6488 7289 M +61 0403477585 E christophe.gaudin@uwa.edu.au
M053, Perth WA 6009 Australia
uwa.edu.au